

Journal of Geophysical Research: Earth Surface**RESEARCH ARTICLE**

10.1002/2015JF003803

Key Points:

- The bed is likely thawed under Greenland's southwestern and northeastern ice drainages
- The bed is likely frozen in Greenland's interior, west of the ice sheet's central ice divide
- The basal thermal state of a third of the Greenland Ice Sheet is poorly constrained

Correspondence to:J. A. MacGregor,
joseph.a.macgregor@nasa.gov**Citation:**

MacGregor, J. A., et al. (2016), A synthesis of the basal thermal state of the Greenland Ice Sheet, *J. Geophys. Res. Earth Surf.*, 121, 1328–1350, doi:10.1002/2015JF003803.

Received 4 DEC 2015

Accepted 19 JUN 2016

Accepted article online 22 JUN 2016

Published online 23 JUL 2016

A synthesis of the basal thermal state of the Greenland Ice Sheet

Joseph A. MacGregor^{1,2}, Mark A. Fahnestock³, Ginny A. Catania^{1,4}, Andy Aschwanden³, Gary D. Clow^{5,6}, William T. Colgan⁷, S. Prasad Gogineni⁸, Mathieu Morlighem⁹, Sophie M. J. Nowicki¹⁰, John D. Paden⁸, Stephen F. Price¹¹, and Hélène Seroussi¹²

¹Institute for Geophysics, University of Texas at Austin, Austin, Texas, USA, ²Now at Cryospheric Sciences Laboratory (Code 615), NASA Goddard Space Flight Center, Greenbelt, Maryland, USA, ³Geophysical Institute, University of Alaska Fairbanks, Fairbanks, Alaska, USA, ⁴Department of Geological Sciences, University of Texas at Austin, Austin, Texas, USA, ⁵U.S. Geological Survey, Denver, Colorado, USA, ⁶Institute of Arctic and Alpine Research, University of Colorado Boulder, Boulder, Colorado, USA, ⁷Department of Earth and Space Science and Engineering, York University, Toronto, Ontario, Canada, ⁸Center for Remote Sensing of Ice Sheets, University of Kansas, Lawrence, Kansas, USA, ⁹Department of Earth System Science, University of California, Irvine, California, USA, ¹⁰Cryospheric Sciences Laboratory, NASA Goddard Space Flight Center, Greenbelt, Maryland, USA, ¹¹Fluid Dynamics Group, Los Alamos National Laboratory, Los Alamos, New Mexico, USA, ¹²Jet Propulsion Laboratory, California Institute of Technology, Pasadena, California, USA

Abstract The basal thermal state of an ice sheet (frozen or thawed) is an important control upon its evolution, dynamics, and response to external forcings. However, this state can only be observed directly at sparse boreholes or inferred conclusively from the presence of subglacial lakes. Here we synthesize spatially extensive inferences of the basal thermal state of the Greenland Ice Sheet to better constrain this state. Existing inferences include outputs from the eight thermomechanical ice-flow models included in the Sea Level Response to Ice Sheet Evolution (SeaRISE) effort. New remote-sensing inferences of the basal thermal state are derived from Holocene radiostratigraphy, modern surface velocity, and Moderate Resolution Imaging Spectroradiometer (MODIS) imagery. Both thermomechanical modeling and remote inferences generally agree that the Northeast Greenland Ice Stream and large portions of the southwestern ice-drainage systems are thawed at the bed, whereas the bed beneath the central ice divides, particularly their west facing slopes, is frozen. Elsewhere, there is poorer agreement regarding the basal thermal state. Both models and remote inferences rarely represent the borehole-observed basal thermal state accurately near NorthGRIP and DYE-3. This synthesis identifies a large portion of the Greenland Ice Sheet (about one third by area), where additional observations would most improve knowledge of its overall basal thermal state.

1. Introduction

A substantial portion of the ongoing change in the flow pattern of the Greenland Ice Sheet (GrIS) is attributed either directly or indirectly to externally forced changes in subglacial processes [e.g., *van de Wal et al.*, 2008; *Andrews et al.*, 2014; *Moon et al.*, 2014]. Nonnegligible basal sliding and deformation of subglacial till (hereafter “basal motion”) both require a thawed basal state. Hence, assessing the present thermal state of the bed of the GrIS, even at the simple level of a binary distinction between a frozen and a thawed bed, could advance our understanding of GrIS dynamics and the importance of temperature-related englacial and subglacial processes [e.g., *Seroussi et al.*, 2013; *Colgan et al.*, 2015; *Poinar et al.*, 2015]. Such knowledge is essential for improving predictions of the future contribution of the GrIS to sea level rise [e.g., *Alley et al.*, 2005; *Price et al.*, 2011; *Nowicki et al.*, 2013].

Multiple borehole-temperature studies within the GrIS interior (>100 km from its margin) have generally reported a frozen ice sheet bed [*Weertman*, 1968; *Gundestrup and Hansen*, 1984; *Cuffey et al.*, 1995; *Dahl-Jensen et al.*, 1998] (Figure 1 and Table 1). However, these boreholes are often located at or near ice divides, where a frozen bed was predicted, so that a longer ice core record (in time) could be recovered. Hence, these boreholes have a sampling bias toward frozen beds. NorthGRIP was an unintended but ultimately invaluable exception to this rule [*Dahl-Jensen et al.*, 1997, 2003]. In contrast, borehole studies closer to the ice sheet margin generally report a thawed bed [*Thomsen et al.*, 1991; *Iken et al.*, 1993; *Lüthi et al.*, 2002, 2015; *Harrington et al.*, 2015].

Because boreholes are inherently sparse compared to the areal extent of an ice sheet, thermomechanical modeling has often been applied to evaluate the thermal state of the GrIS bed [*Jenssen*, 1977; *Funk et al.*, 1994; *Huybrechts*, 1994, 1996; *Greve and Hutter*, 1995; *Calov and Hutter*, 1996; *Greve*, 1997, 2005; *Tarasov*

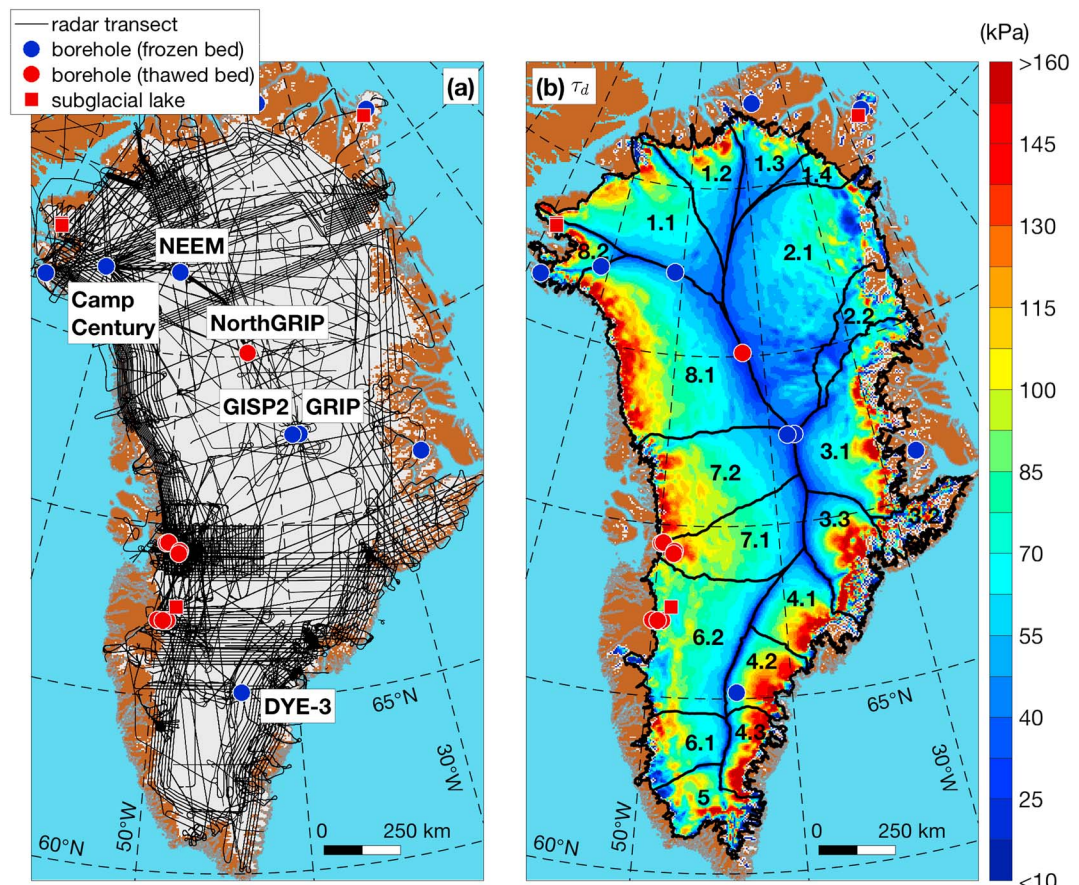


Figure 1. (a) Map of Greenland showing the spatial coverage of 1993–2013 radar-sounding data used in this study (same as MacGregor et al. [2015a]), the basal thermal state of deep boreholes, and the locations of known subglacial lakes. Table 1 lists the sources for the borehole data and subglacial lake locations. (b) Ice-drainage systems (IDS) of the GrIS, as delineated and labeled by Zwally et al. [2012], overlaid on the driving stress τ_d .

and Peltier, 2003; Marshall, 2005; Heimbach and Bugnion, 2009; Rogozhina et al., 2011, 2012, 2016; Aschwanden et al., 2012; Brinkerhoff and Johnson, 2013; Petrunin et al., 2013; Seroussi et al., 2013; Poinar et al., 2015]. These models generally predict what we term a “scalloped frozen core” for the GrIS, i.e., a central region where the bed is frozen, surrounded by thawed regions that can extend from the ice sheet margin to hundreds of kilometers inland. These models typically agree with contemporaneous borehole-temperature measurements, but there is less obvious intermodel agreement elsewhere, and their basal temperature outputs have yet to be synthesized. In terms of importance for constraining the basal thermal state, these studies have variously emphasized the multimillennial memory of ice sheets, the spatiotemporal variability of key boundary conditions (accumulation rate and geothermal flux), conservation of energy in a polythermal ice sheet, model initialization and fidelity to the flow, and geometry of the modern GrIS. Inferences of basal motion from surface-velocity patterns also suggest a spatially heterogeneous GrIS basal thermal state, similar to that predicted by thermomechanically coupled models [Rignot and Mouginot, 2012; Sergienko et al., 2014].

Studies of internal and basal reflections recorded by radar sounding have also produced evidence of spatiotemporally variable basal melting, freezing, and motion beneath the GrIS [Fahnestock et al., 2001; Dahl-Jensen et al., 2003; Oswald and Gogineni, 2008, 2012; Palmer et al., 2013; Bell et al., 2014; Christianson et al., 2014; Keisling et al., 2014; Wolovick et al., 2014]. With the recent exception of Rogozhina et al. [2016], none of this radar-derived information regarding the basal thermal state has been synthesized with thermomechanical models of the entire GrIS, leaving a gap between contributions to our knowledge of its basal thermal state from radar and modeling.

Given the range of existing estimates of the present basal thermal state of the GrIS, both additional approaches to resolving this state and a synthesis of existing estimates are warranted. In this study, we

Table 1. Boreholes and Known Subglacial Lakes Used to Evaluate Inferences of the Thermal State of the Bed of the GrIS

Site	Latitude (°N)	Longitude (°W)	Ice Thickness (m)	Basal Temperature (Observed/Corrected ^a , °C)	Reference
Boreholes					
Interior					
Camp Century	77.18	61.13	1387	-13.0/-11.8	Weertman [1968]
DYE-3	65.18	43.82	2037	-13.2/-11.4	Gundestrup and Hansen [1984]
GISP2	72.60	38.50	3053	-9.2/-6.6	Cuffey et al. [1995]
GRIP	72.58	37.64	3029	-8.6/-6.0	Bender et al. [2010]
NEEM	77.45	51.06	2538 ^b	-3.5/-1.3	MacGregor et al. [2015b] ^c
NorthGRIP	75.10	42.32	3085	~ -2.3/0	Dahl-Jensen et al. [2003] ^d
Southwestern margin					
Swiss Camp	69.57	49.28	N/A	T	Thomsen et al. [1991]
Jakobshavn Isbræ	~69.19	~48.77	1540–1630	-1.1/0	Iken et al. [1993]
Jakobshavn Isbræ	69.24	48.69	830	-0.6/0	Lüthi et al. [2002]
Paakitsoq	69.45	49.88	614–624	-0.5/0	Lüthi et al. [2015]
Isunnguata Sermia	~67.19	~49.52	92–821	-0.7--0.1/0	Harrington et al. [2015]
Peripheral ice caps					
Renland	71.30	26.72	324	F	Hansson [1994]
Hans Tausen	82.50	37.52	345	F	Madsen and Thorsteinsson [2001]
Flade Isblink	81.29	15.70	540	F	Lemark [2010]
Subglacial lakes					
Northwestern margin	~77.92	~68.89	757–809	T	Palmer et al. [2013]
Southwestern margin	67.61	48.69	1200	T	Howat et al. [2015]
Flade Isblink	81.16	16.58	540	T	Willis et al. [2015]

^a“Corrected” means corrected for pressure-melting using local ice thickness. Where basal temperatures were not measured directly but confidently inferred, we give the basal thermal state as either frozen (F) or thawed (T).

^bNote that ice thickness at NEEM was reported incorrectly by MacGregor et al. [2015a, 2015b] as 2561 m.

^cThe deepest measured temperature was -3.56°C at 2537.36 m. An additional 0.63 m of silty ice was drilled following this measurement, resulting in an extrapolated basal temperature of -3.54°C.

^dDahl-Jensen et al. [2003] estimated a basal temperature of -2.4°C based on the deepest measured temperature available at the time (-7.8°C at 2880 m). Following further drilling, the temperature measured at 2992.6 m was -5.17°C. Drilling eventually reached the bed, but the basal temperature was not measured there. Here we use the newer, deeper temperature measurement and the observed vertical temperature gradient (31 mK m⁻¹) to estimate the basal temperature.

produce multiple new estimates of the GrIS basal thermal state and synthesize these results with earlier estimates from three-dimensional (3-D) thermomechanical ice sheet models. Our new estimates are derived from radiostratigraphy-constrained ice-flow modeling and analysis of surface velocity and imagery. Our goal is to map the portions of the GrIS where these methods agree that the bed is frozen or thawed versus where there is poor agreement between these methods.

2. Data and Methods

2.1. 3-D Thermomechanical Modeling of Basal Temperature

To quantitatively evaluate basal temperatures for the entirety of an ice sheet, numerical thermomechanical modeling is required. Such modeling explicitly solves the coupled mass-, momentum-, and energy-conservation equations over the entire ice sheet, given certain boundary conditions. We evaluate the basal temperature outputs from the eight 3-D thermomechanical models of the GrIS included in the Sea Level Response to Ice Sheet Evolution (SeaRISE) effort described by Nowicki et al. [2013]. That study also described the models’ varied resolutions, initializations, thermodynamic representations, and boundary conditions in detail. More 3-D model representations of the present basal thermal state of the GrIS exist than this ensemble of SeaRISE models alone. We opted to use the SeaRISE ensemble only because it enables a straightforward evaluation of multiple models to which similar modern boundary conditions were applied. Several trade-offs presently exist between different types of models, such as those that are initialized across glacial-interglacial cycles [e.g., Rogozhina et al., 2011] versus those that assimilate modern observations (e.g., Ice Sheet System Model (ISSM) [Seroussi et al., 2013]). We set aside the myriad issues facing such comparisons and focus instead on simply evaluating the present agreement between a relatively large number of models.

We consider only the SeaRISE basal temperature fields at the end of their 100 year control runs (“CC” in the nomenclature of Nowicki et al. [2013]), because these fields represent relaxed states characteristic of present

day and with no prescribed additional forcings. We correct all modeled basal temperatures (T_{bed}) to be relative to the pressure-melting point (T'_{bed}) using the ice-thickness field for each model at the end of its control run and a value of $8.7 \times 10^{-4} \text{ K m}^{-1}$ for the rate of decrease in the pressure-melting point with increasing ice thickness [Cuffey and Paterson, 2010].

For three of the SeaRISE models (Community Ice Sheet Model (CISM), Ice Sheet System Model (ISSM), and Parallel Ice Sheet Model (PISM)), we use subsequent revisions to the models described below. All models use an enthalpy formulation for conservation of energy that accounts for the latent heat of liquid water within temperate ice (i.e., ice at the pressure-melting point) [Aschwanden et al., 2012]. For the instance of CISM employed here (v2.0), the momentum balance is still based on the 3-D first-order Stokes approximation (the “Blatter-Pattyn” approximation), but the equations are now formulated following the variational approach of Dukowicz et al. [2010] and discretized using finite elements on a fixed, regular grid. Model tuning follows that for SeaRISE [Price et al., 2011], but the spin-up has been extended to last 350 ka to better approximate equilibrium englacial temperatures. The instance of ISSM we use here is the same as the steady state run described by Seroussi et al. [2013]. This model also used the SeaRISE data sets for several boundary conditions but adjusted geothermal flux to better match borehole constraints. This model instance assumes thermal steady state, although its englacial temperatures compare favorably with radar-inferred depth-averaged temperatures [MacGregor et al., 2015b]. The instance of PISM we use here was initialized using the “paleoclimate” method described by Aschwanden et al. [2013], and the prescribed geothermal flux follows Shapiro and Ritzwoller [2004], as for the SeaRISE experiments.

2.2. Basal Melting and Motion From Radiostratigraphy

The local rate of basal melting and/or motion necessary to explain radar-observed depth–age relationships (dated radiostratigraphy) can be inferred from ice-flow modeling of varying degrees of complexity [e.g., Fahnestock et al., 2001; Dahl-Jensen et al., 2003; Keisling et al., 2014; Wolovick et al., 2014; Wolovick and Creyts, 2016; Koutnik et al., 2016]. Hence, analysis of dated radiostratigraphy can inform our understanding of the basal thermal state across large regions of an ice sheet.

Here we extend the one-dimensional (1-D; vertical), steady state ice-flow modeling approach of Fahnestock et al. [2001] to produce estimates of the local basal melt rate \dot{m} , basal shear layer thickness h , and shape factor ϕ that best match Holocene radiostratigraphy across the GrIS. These three quantities are derived from two analytical 1-D ice-flow models (Nye + melt, Dansgaard–Johnsen) that make distinct assumptions about flow within the ice column. Figure 2 illustrates these two models schematically. To constrain these 1-D models, we use the same GrIS-wide dated radiostratigraphy developed and described by MacGregor et al. [2015a] and further investigated by MacGregor et al. [2015b, 2016]. Figure 1a shows the spatial coverage of the radar-sounding data.

To estimate \dot{m} , we use the “Nye + melt” ice-flow model described by Fahnestock et al. [2001], which predicts the following depth–age relationship:

$$a_{N+\dot{m}}(z) = \frac{H}{\dot{m} - b} \ln \left(\left[\frac{H-z}{H} \left(1 - \frac{\dot{m}}{b} \right) \right] + \frac{\dot{m}}{b} \right), \quad (1)$$

where $a(z)$ is the age a of the ice at ice-equivalent depth z , H is the ice thickness, and b is the surface-accumulation rate. In this first 1-D ice-flow model, the ice column is assumed to deform in pure shear only (uniform horizontal velocity with depth).

The shape factor ϕ is the ratio between the depth-averaged horizontal speed of the ice column \bar{u} and its surface speed u_s [Cuffey and Paterson, 2010]:

$$\phi = \frac{\bar{u}}{u_s}. \quad (2)$$

Where ϕ approaches unity, vertical shear in the ice column is negligible; therefore, the rate of basal motion u_b must approach u_s , and the ice deforms in pure shear, as in the Nye + melt model. Where $\phi < 1$ ice flow must be also accommodated by simple shear [Cuffey and Paterson, 2010]. Assuming that the Glen’s flow law exponent $n = 3$ and a uniform rate factor for the ice column, a lower limit for ϕ is approximately $(n+1)/(n+2) = 0.8$. Following MacGregor et al. [2016], the geometric relationship between ϕ and h is

$$\phi = 1 - \frac{h}{2H}. \quad (3)$$

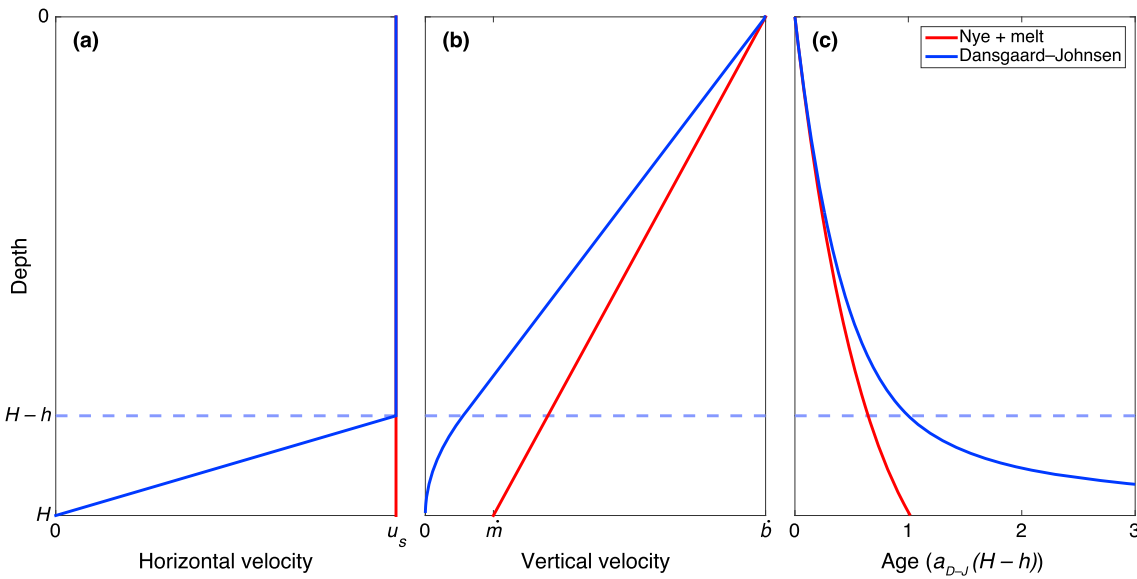


Figure 2. Schematic of Nye + melt (red) and Dansgaard–Johnsen (blue) 1-D ice-flow models in terms of their relative depth profiles (normalized by ice thickness H) of (a) horizontal velocity, (b) vertical velocity, and (c) age. The underlying physical assumptions regarding the depth profiles of horizontal velocity for each model lead to the depth–age relationships shown. This latter modeled quantity (age) is that which we compare to observations (dated radiostratigraphy) to then infer the basal melt rate (\dot{m}) and shear layer thickness (h). In this schematic, age is normalized by its value at $H - h$ in the Dansgaard–Johnsen model.

We estimate h (and hence ϕ) using a second 1-D ice-flow model, introduced by *Dansgaard and Johnsen [1969]*, which predicts the following depth–age relationship:

$$a_{D-J}(z) = \begin{cases} \frac{2H-h}{b} \ln\left(\frac{2H-h}{2(H-z)-h}\right), & z \leq H-h, \\ a_{D-J}(H-h) + \frac{2H-h}{b} \ln\left(\frac{h}{H-z}-1\right), & z > H-h. \end{cases} \quad (4)$$

In this second 1-D ice-flow model, the ice column is assumed to be deforming in pure shear only where $z \leq H - h$ (uniform vertical strain rate), but also in simple shear, where $z > H - h$, i.e., within the basal shear layer (linearly decreasing vertical strain rate).

To estimate either \dot{m} or h (and hence ϕ) from a dated radiostratigraphy using the above models, we must also constrain \dot{b} , a surface boundary condition of broad glaciological value but which only indirectly and slowly affects the basal thermal state. For a plausible range of values, both models are overall more sensitive to \dot{b} than to \dot{m} or h . Both 1-D ice-flow models are explicitly steady state. Hence, following *Fahnestock et al. [2001]* and *MacGregor et al. [2016]*, we restrict these models to only use reflections that are 9 ka old or less (the last three quarters of the Holocene epoch), when \dot{b} was stable across millennial time scales. Following *MacGregor et al. [2016]*, we require at least four dated reflections within each 1-km along-track bin to estimate \dot{m} and h as the best fit parameters from a nonlinear unconstrained minimization of χ^2 statistic:

$$\chi^2 = \sum_{i=1}^N \left(\frac{a_{\text{obs}}^i - a_{\text{model}}^i}{\tilde{a}_{\text{obs}}^i} \right)^2, \quad (5)$$

where N is the number of Holocene-dated reflections; a_{obs}^i and \tilde{a}_{obs}^i are the age and age uncertainty of the i th dated reflection, respectively; and a_{model}^i is the modeled age of that same reflection, calculated using its depth and either equation (1) or (4). Confidence bounds (95%) for both model parameters are estimated using $\Delta\chi^2$ distributions. We grid along-track values using ordinary kriging with parameters similar to *MacGregor et al. [2015a, 2016]*.

These two 1-D ice-flow models use the same data to produce distinct but related inferences of basal melting or motion. For example, a negative value of h (and hence $\phi > 1$) is nonphysical, indicating that \dot{m} is positive (implying basal melting) and possibly greater than \dot{b} [*Fahnestock et al., 2001*]. While these ice-flow models are

relatively unsophisticated and nonunique, they are also relatively simple to evaluate and interpret. *Dahl-Jensen et al.* [2003] introduced a more sophisticated 1-D ice-flow model that is essentially a combination of the above two models ("Dansgaard–Johnsen + melt"). While this model is more physically complete, we do not consider it here as we found separately that simultaneously solving for its four parameters (b , m , h , and u_b/u_s) results in less well constrained solutions than the two models that we consider here.

Separate from the steady state assumption, 1-D modeling of radiostratigraphy is not appropriate for the entirety of an ice sheet, because horizontal gradients in ice flow can alter locally observed depth–age relationships substantially [*Waddington et al.*, 2007; *Koutnik et al.*, 2016]. Hence, the strain history of the particles that form observed isochrones may differ from their apparent history at their present location. Following *MacGregor et al.* [2016], we restrict our interpretation of radiostratigraphy-inferred values of m , h , and ϕ to the portion of the GrIS where we consider the local layer approximation to be acceptable for reflections younger than 9 ka, i.e., the region where depth–age relationships may be represented reasonably by 1-D models that neglect horizontal gradients in ice flow. This region encompasses the majority of the GrIS (71% by area).

2.3. Basal Motion From Surface Properties

2.3.1. Surface Velocity

Fast ice flow is widely accepted as an indicator of basal motion and hence of a thawed bed. Because creep deformation also contributes to ice flow, u_s is not equal to u_b . A simple estimate of the maximum flow speed due to internal ice deformation only is therefore valuable for constraining where basal motion is likely contributing to the observed pattern of u_s and hence where the bed is thawed. We generate this estimate by calculating the surface speed due to ice deformation (u_{def}) for an ice column that is entirely at the pressure-melting point (i.e., temperate), following *Cuffey and Paterson* [2010] as

$$u_{\text{def}} = \frac{2\bar{\alpha}}{n+1} \tau_d^n H, \quad (6)$$

where $\bar{\alpha}$ is the rate factor for temperate ice, $\tau_d = \rho_{\text{ice}} g H \alpha$ is the gravitational driving stress (Figure 1b), ρ_{ice} is the mean density of the ice column (900 kg m^{-3}), g is the acceleration due to gravity (9.81 m s^{-2}), and α is the along-flow surface slope. For H , we use the gridded field and its uncertainty from *Morlighem et al.* [2014]. We assume that the uncertainty in u_{def} is due to uncertainty in $\bar{\alpha}$ and H only and propagate their uncertainties into lower and upper bound estimates of u_{def} .

For temperate ice, a synthesis of reported values by *Cuffey and Paterson* [2010] suggests that $\bar{\alpha} = 2.4 \times 10^{-24} \text{ Pa}^{-3} \text{ s}^{-1}$, which is consistent with borehole-deformation measurements of the GrIS [*Ryser et al.*, 2014a]. For polar ice experiencing simple shear, they also suggest an enhancement factor $E \geq 2$ to account for fabric development and for softer ice from the Last Glacial Period [*Paterson*, 1991; *Lüthi et al.*, 2002]. Such ice can greatly influence ice flow [e.g., *Ryser et al.*, 2014a], although it generally constitutes a smaller portion of the ice column [*MacGregor et al.*, 2015a]. Hence, we ignore E in our calculation of u_{def} but assign $\bar{\alpha}$ a relative uncertainty of 25%.

Rignot and Mouginot [2012] also calculated u_{def} for the GrIS and determined that, when attempting to match u_s and u_{def} in the northern GrIS interior, the best fit value for $\bar{\alpha}$ was $1.2 \pm 0.2 \times 10^{-24} \text{ Pa}^{-3} \text{ s}^{-1}$. This value is half of that which we assume and equivalent to a depth-averaged temperature of -3.8°C . However, our approach does not require the assumption that any particular region of the ice sheet is frozen at its base. Of course, the whole of the GrIS is not temperate (e.g., Figure 1), and the 3-D models also produce estimates of the englacial temperature. The advantage of our particular approach, as compared to more sophisticated thermomechanical modeling, is simplicity of interpretation. We consider the large-scale flow field of the whole ice sheet only, rather than attempting to interpret the detail and significance of driving stress variability in any given region (e.g., Figure 1b [*Sergienko et al.*, 2014]).

To determine the direction of α , we first use a composite map of Greenland surface velocity (I. Joughin, personal communications, 2015) developed using the same methodology described by *Joughin et al.* [2010]; i.e., it is derived from a combination of interferometric synthetic aperture radar analysis and speckle tracking of spaceborne imagery. This composite field is derived from 1995 to 2013 synthetic aperture radar data, and it is the same as that used by *MacGregor et al.* [2016]. In the slower flowing interior, ionospheric noise limits the quality of satellite-derived flow azimuths. Therefore, in this region ($\leq 100 \text{ m a}^{-1}$) we progressively weight the

Table 2. Discriminating Characteristics of the Basal Thermal State From Each Method

Method	Implies a Frozen Bed	Implies a Thawed Bed
3-D thermomechanical model ^a	$T'_{\text{bed}} < -0.05^{\circ}\text{C}$	$T'_{\text{bed}} > -0.05^{\circ}\text{C}$
Shape factor from radiostratigraphy	$\phi < [(n+1)/(n+2)]^b$	$\phi > 1$
Maximum deformation speed	N/A	$u_s > u_{\text{def}}$
Surface texture	N/A	Discernible surface undulations

^aBy setting a cutoff for T'_{bed} at -0.05°C , we are effectively assuming that the uncertainty in these models is 0.05 K, due to numerical approximations. For the lower and upper bound estimates of the basal thermal state from the 3-D models (cold and warm biases in Figures 10c and 10d, respectively), we use cutoffs of 0°C and -0.5°C , respectively.

^bAssuming $n = 3$.

surface-velocity azimuth toward the direction of the surface-elevation gradient of the Greenland Ice Mapping Project digital elevation model [Howat *et al.*, 2014]. This weighting depends exponentially on the magnitude and relative uncertainty of the local surface speed. We rotate the projected surface-velocity field onto this weighted flow azimuth, which improves representation of ice flow in the GrIS interior. This weighted flow azimuth is used to determine the magnitude of α .

2.3.2. Surface Texture

Fast basal motion can effectively transmit large-scale ($\sim 1\text{--}20H$ horizontally) bedrock topographic features into the ice sheet [Gudmundsson, 2003; Hindmarsh *et al.*, 2006; Bell *et al.*, 2007; De Rydt *et al.*, 2013; Ryser *et al.*, 2014b]. At the subaerial ice surface, this basal motion can manifest as transverse-to-flow surface undulations. Hence, the surface texture of an ice sheet is related indirectly to the slip ratio $s = u_b/u_{\text{def}}$. Where $s > > 1$ (equivalent to $\phi \rightarrow 1$), the surface texture is expected to be much rougher than where $s \leq 1$ [De Rydt *et al.*, 2013] and is an indirect indicator of a thawed bed.

The surface texture of the GrIS was explored by Scambos and Haran [2002] using an Advanced Very High Resolution Radiometer (AVHRR) mosaic and in greater detail along a few transects by van der Veen *et al.* [2009]. Here we use the Moderate Resolution Imaging Spectroradiometer (MODIS) Mosaic of Greenland (MOG) to analyze the texture of the subaerial ice surface of the GrIS [Haran *et al.*, 2013]. MODIS imagery is well suited to surface-texture analysis because of its relatively high spatial and radiometric resolutions and because of the high-pass filtering that can be applied to this imagery to enhance visibility of surface texture. MOG is posted at 100 m, with an effective resolution of ~ 200 m, so it offers an approximately fivefold improvement in spatial resolution over the AVHRR mosaic studied by Scambos and Haran [2002]. We examine MOG at a small scale ($\sim 1:200,000$) with a narrow, localized contrast stretch (~ 8 bit) and delineate the ice sheet transition between a relatively smooth surface and prominent surface undulations. We assume that this transition in surface texture represents a boundary where $s > > 1$ downstream. This transition is traced twice, once as described above ("standard") and a second time using a stricter visual criterion for the onset of surface undulations ("conservative").

2.4. Synthesizing Basal Thermal State Estimates

We synthesize the multiple methods of constraining the basal thermal state across the GrIS described above by simply assessing where each of the above independent methods produces a clear signal regarding this state. Table 2 lists the bounds used to discriminate between a frozen and thawed bed for each method. We initialize a 5 km gridded ice sheet mask S to zero. For each method at each grid point, if a signal exists for a frozen (thawed) bed, then -1 (+1) is added to S . Because the radiostratigraphic constraints are not independent of each other, ϕ is the only radiostratigraphic constraint used to determine S .

If a given method does not yield an unambiguous signal regarding the basal thermal state, then S is not adjusted there based on that method. For example, where $[(n+1)/(n+2)] < \phi < 1$, ϕ does not clearly distinguish between a frozen and a thawed bed. We do not weight any of the methods with respect to each other. Prior to but following the same procedure as for S , a separate mask is generated using the 3-D thermomechanical model outputs, each weighted equally. In this manner, each independent method contributes to an unbiased synthesis of the GrIS basal thermal state.

Based on confidence bounds or uncertainty estimates for each of the four methods described above and their discriminating characteristics (Table 2), two additional instances of S are generated: a cold-bias instance and a warm-bias instance (S_{cold} and S_{warm} , respectively). We then generate a new mask (L) that synthesizes the agreement between the different methods and represents the likely thermal state of the bed of the GrIS.

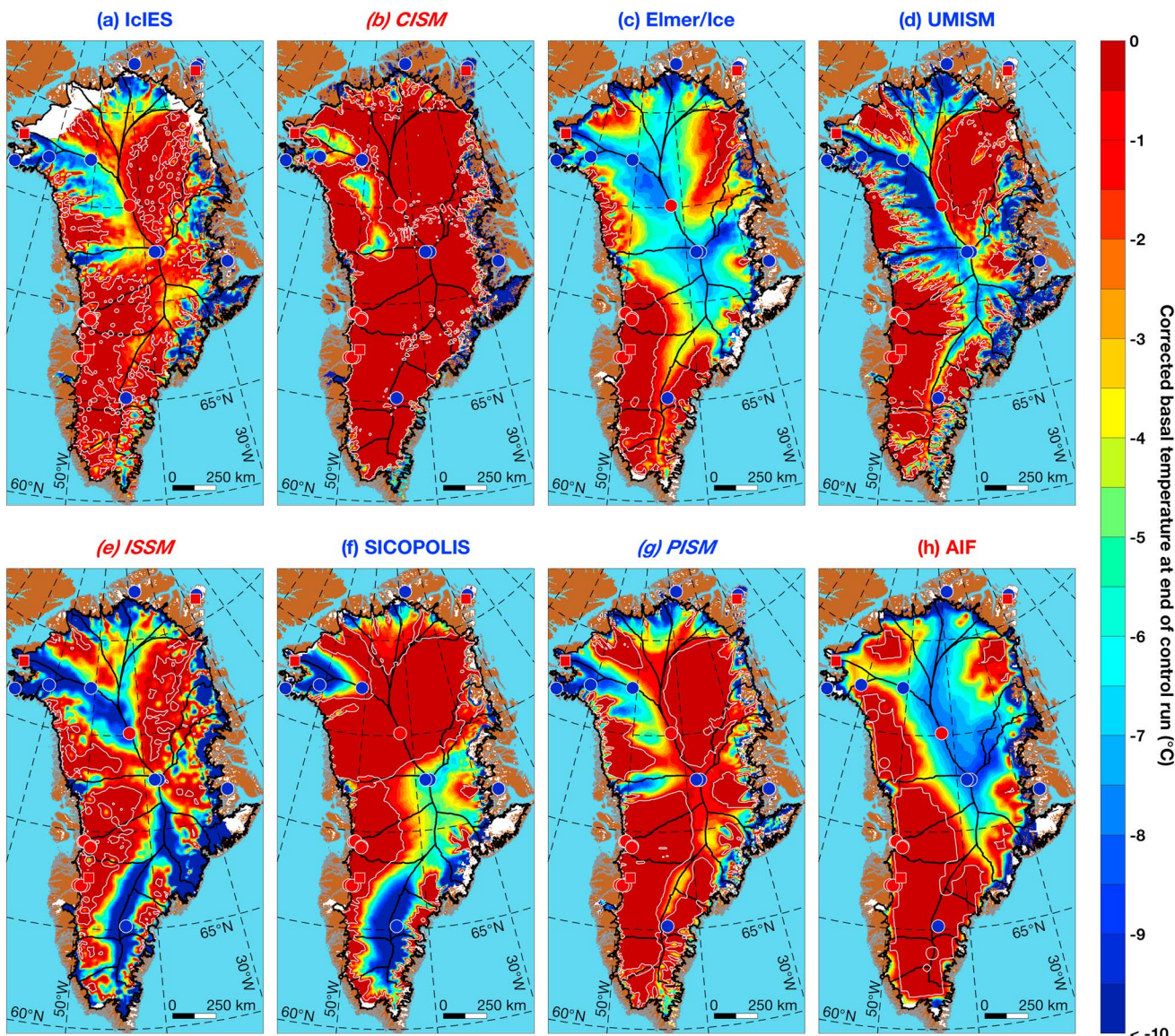


Figure 3. Modeled pressure-melting-corrected basal temperature across the GrIS (T'_{bed}) from the end of the SeaRISE control-run experiments. The (b) CISM, (e) ISSM, and (g) PISM instances (model names italicized) are improved relative to those included in the SeaRISE effort. Models with blue titles were initialized using various paleoclimatic forcings, whereas models with red titles assimilated modern data to determine their geometry and dynamics. The IcIES model is also slightly revised from that used in the SeaRISE experiments, and the AIF model uses a cubic exponent for the power law relationship between basal motion and friction. White contours represent where $T'_{\text{bed}} = -0.05^{\circ}\text{C}$, the temperature cutoff above which we assume the bed is thawed (Table 2).

This mask is somewhat analogous to the analysis performed by [Pattyn \[2010\]](#) using multiple instances of a thermomechanical model of the Antarctic Ice Sheet. L is also initialized to zero and then assigned -1 ($+1$), representing a frozen (thawed) bed where at least two of the three instances of S agree on the basal thermal state (sign of S), regardless of their degree of agreement in this state (magnitude of S). If only two instances of S agree, then the assignment is made only if the other instance does not suggest the opposite basal thermal state.

We assume that regions of the bed where $L=0$ (uncertain) that are surrounded by likely thawed or frozen bed ($L=-1$ or $+1$, respectively) are more likely than not to possess the same basal thermal state as their surroundings. Following this reasoning, we reassign uncertain “holes” less than 10 grid cells in size ($\leq 250 \text{ km}^2$) with their surrounding basal thermal state. Similarly, in regions where $L=0$, we reassign likely frozen or thawed “holes” of the same limited size to $L=0$.

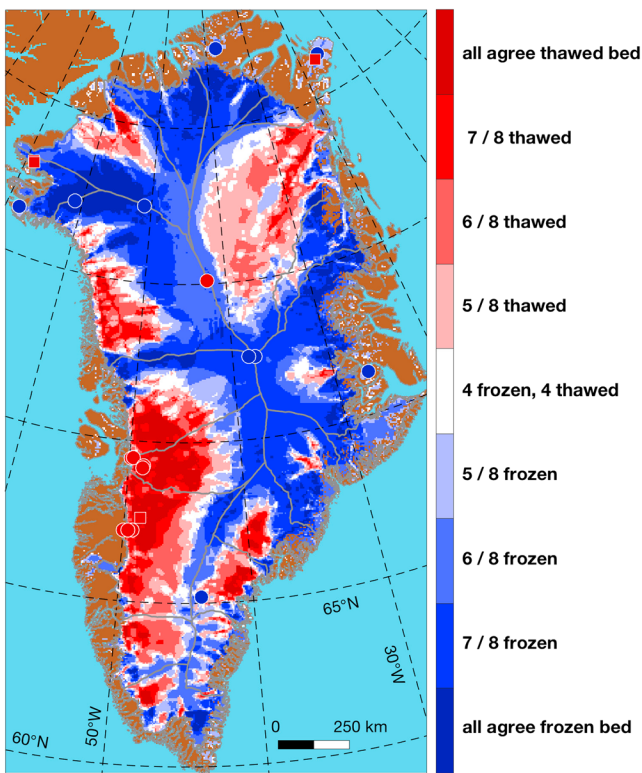


Figure 4. Agreement in T'_{bed} between the SeaRISE control-run experiments and updated models shown in Figure 3, assuming that the bed is thawed if a model reports $T'_{\text{bed}} \geq -0.05^{\circ}\text{C}$.

2.5. Borehole Observations

2.5.1. Temperature

To qualitatively evaluate the four methods' inferences of the basal thermal state of the GrIS and our synthesis, we use the temperature-depth profiles measured in the six deep boreholes that have associated ice cores (Camp Century, DYE-3, GISP2, GRIP, NEEM, and NorthGRIP). Additional full-thickness borehole-temperature profiles exist for the GrIS from its southwestern margin and elsewhere along the margin, and these are also included in our analysis. Figure 1 maps the locations of these boreholes in Greenland, and Table 1 summarizes their key features, including their measured and pressure-melting-adjusted ("corrected") basal temperatures (i.e., relative to the local pressure-melting point). Subglacial lakes are taken as indicators of a thawed bed, and the locations of the few known subglacial lakes beneath the GrIS are also shown in Figure 1. For completeness, we also show comparable inferences of basal temperatures for Greenland's peripheral ice caps.

2.5.2. Inclinometry

To evaluate radiostratigraphic inferences of basal motion, measured depth profiles of horizontal velocity are required. These profiles are derived by integrating borehole-inclinometry data collected at three boreholes: Camp Century [Gundestrup *et al.*, 1993], DYE-3 [Dahl-Jensen and Gundestrup, 1987], and GISP2 [Bender *et al.*, 2010]. Borehole-deformation studies by Lüthi *et al.* [2002] and Ryser *et al.* [2014a], within and near Jakobshavn Isbræ, are too far (>50 km) from radiostratigraphic inferences of basal motion for such a comparison to be reliable.

3. Results

3.1. The 3-D Thermomechanical Model Estimates of the Basal Thermal State

Figure 3 shows the eight 3-D thermomechanical model estimates of GrIS basal temperatures, and Figure 4 synthesizes these estimates. Figure 3 shows that there is a diversity of 3-D estimates of GrIS basal thermal state, but because they are weighted equally when synthesized, that diversity is muted in Figure 4. From Figure 3, there is no clear relationship between the predicted basal thermal state and whether the model assimilates modern observations or is initialized using various paleoclimatic forcings.

The region of largest agreement that the bed is thawed is in southwestern Greenland (ice-drainage systems—hereafter IDS—6.2, 7.1, and 7.2; following Figure 1b), which also has the most extensive ablation zone, but this agreement also extends well into its accumulation zone. These models also predict that two southeastern drainage systems (IDS 4.1 and 4.2) are mostly thawed, as well as the northwestern portion of the GrIS that faces Baffin Bay (IDS 7.2 and 8.1) and the main trunks of Humboldt and Petermann Glaciers in northwestern Greenland (IDS 1.1). The large ice-drainage system (IDS 2.1) that includes the Northeast Greenland Ice Stream (NEGIS; hereafter the "NEGIS system") is sometimes predicted to be thawed but not as consistently as the aforementioned regions.

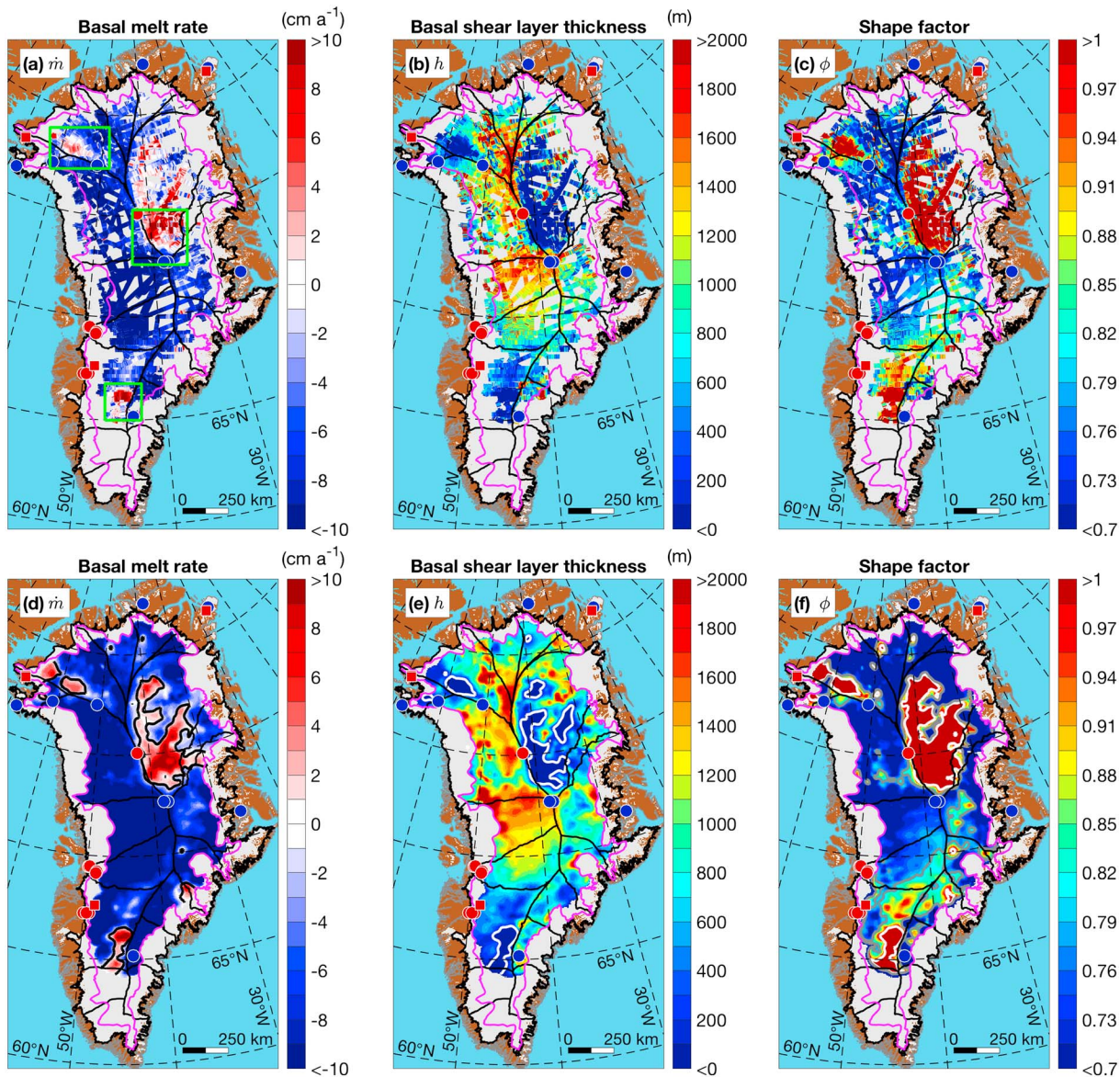


Figure 5. (a–c) Along-track and (d–f) gridded apparent basal melt rate \dot{m} (ice equivalent), basal shear layer thickness h , and shape factor ϕ across the GrIS, respectively. The first of these quantities was derived using the Nye + melt model (equation (1)), whereas the second two were derived using the Dansgaard–Johnsen model (equation (4)). Magenta line represents the outermost limit of acceptability of 1-D ice-flow modeling for ≤ 9 ka old radiostratigraphy [MacGregor et al., 2016]. Black outline in Figure 5b and white outline in Figure 5d represent $\dot{m} = 0$ and $h = 0$ contours, respectively. In Figure 5f, white (gray) solid line is $\phi = 1$ (0.8) contour. Confidence regions for these outlines, based on gridding of the 95% confidence bounds for along-track values, have similar extents. Green boxes in Figure 5a outline regions shown in Figure 6.

Only the northwestern extensions of the central ice divides are predicted consistently to be frozen to the bed, particularly between Camp Century and NEEM. Elsewhere, ice divides are generally predicted to be frozen, but not uniformly so, as in the vicinity of NorthGRIP and DYE-3. The northernmost reach of the GrIS is expected to be frozen (most of IDS 1.2, 1.3, and 1.4), as is the central half of the eastern GrIS coastline (IDS 3.1) and a substantial portion of the interior west of the central ice divide.

The NEGIS system and the GrIS south of $\sim 65^{\circ}\text{N}$ are the regions of greatest uncertainty in the 3-D modeled basal thermal state. Elsewhere, the location of the along-flow transition from a frozen to a thawed bed (if there is one) is rarely well constrained and often spans >100 km in the along-flow direction.

3.2. Radiostratigraphic Constraints on the Basal Thermal State

Figures 5 and 6 show the 1-D model estimates of \dot{m} , h , and ϕ across the GrIS. These quantities are related to each other, as expected [Fahnestock et al., 2001]. Rather than restrict calculation of \dot{m} to regions where $h < 0$,

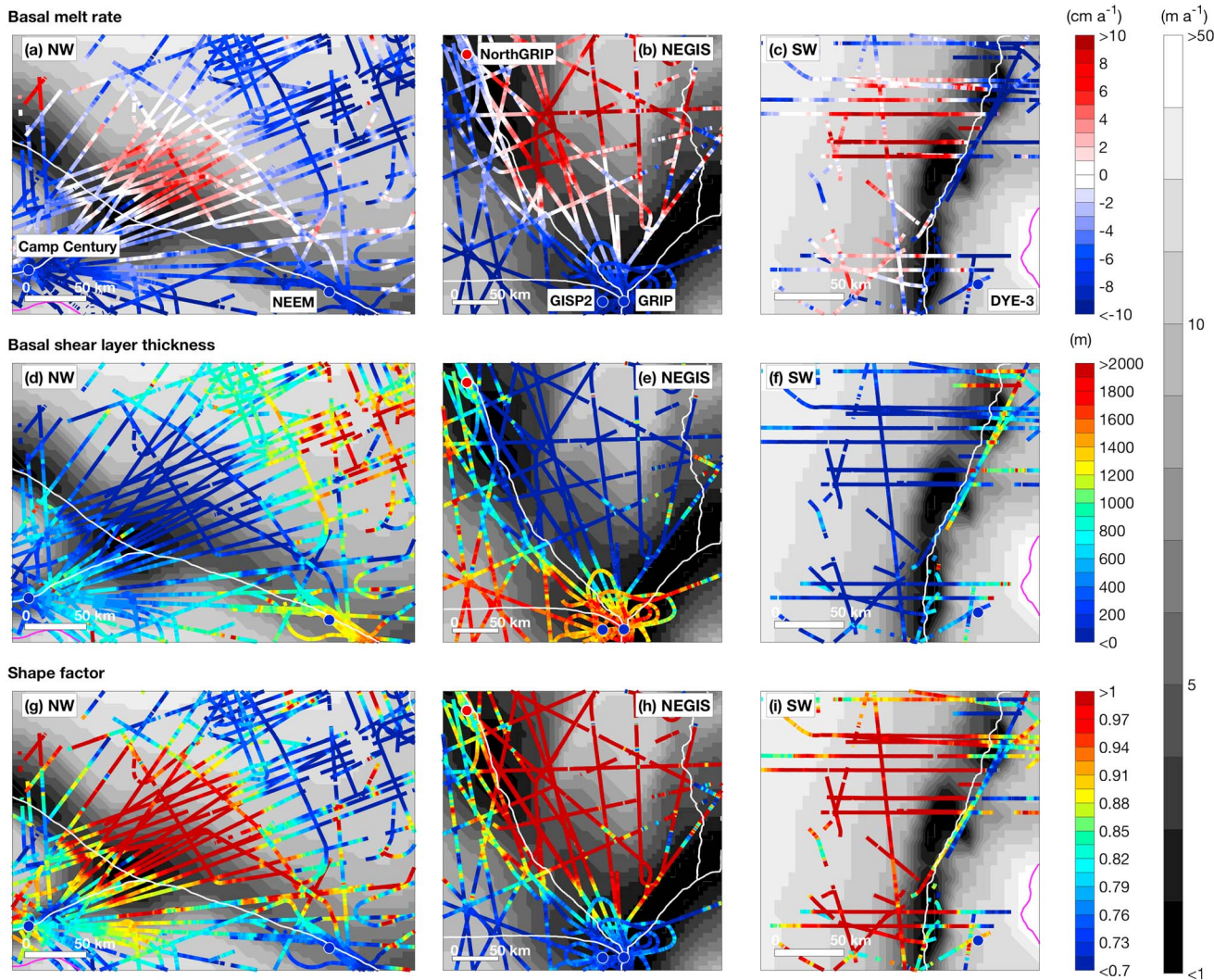


Figure 6. Along-track (a–c) basal melt rate \dot{m} , (d–f) basal shear layer thickness h , and (g–i) shape factor ϕ in the (Figures 6a, 6d, and 6g) NW, (Figures 6b, 6e, and 6h) NEGIS, and (Figures 6c, 6f, and 6i) SW regions, respectively. Background gray scale is the observed surface speed. White lines are the ice-drainage divides, and magenta line is the downstream limit of reliable 1-D modeling.

as was done by Fahnestock *et al.* [2001], here we simply estimate all quantities where sufficient traced Holocene radiostratigraphy exists and restrict our interpretation to the region where 1-D modeling of such radiostratigraphy is acceptable.

Evidence of significant apparent basal melting ($\dot{m} > 0$) is restricted primarily to three portions of the GrIS. The largest of these three regions includes most of the NEGIS system, first identified by Fahnestock *et al.* [2001] using nearly the same methodology. The other two smaller regions of significant apparent basal melt are in the northwest (NW; IDS 1.1) and southwest (SW; IDS 6.2) ice-drainage systems. They are of comparable size and have not been identified previously as possessing significant basal melting. Both regions are relatively near (<100 km) to frozen boreholes.

The NW region of basal melting is north of the ice divide along which both Camp Century and NEEM are located. It is composed of two subregions, one of which is approximately equidistant from those two boreholes and is well constrained by the spatial coverage of the radiostratigraphy. The other region is farther northwest and reaches the marginal limit of our 1-D modeling. Gridding suggests that this basal-melting signal nearly reaches the ice margin (Figure 5d), but we consider this inference to be speculative because of the sparse along-track coverage (Figure 6a). The SW region of basal melting is west of DYE-3, on the other side of

the central ice divide. It is also remarkable because the basal temperature at DYE-3 was $<-10^{\circ}\text{C}$ (Table 1), <50 km southeast of this region's eastern edge.

We find that $\dot{m} < 0$ in the immediate vicinity (≤ 5 km) of all interior boreholes. This pattern is qualitatively consistent with borehole-measured basal temperatures, except for NorthGRIP. We infer basal melting at a rate of less than 1 cm a^{-1} within 15 km of NorthGRIP but not at the borehole itself. This result differs slightly from that of *Dahl-Jensen et al.* [2003], who used a Dansgaard–Johnsen + melt model in conjunction with an along-divide radar-sounding transect and found that \dot{m} typically exceeded 0.5 cm a^{-1} along the flow line immediately upstream of NorthGRIP, which agreed with borehole observations. This discrepancy emphasizes the limitations of 1-D ice-flow modeling and the need to focus on larger-scale patterns in these 1-D inferences of \dot{m} (and hence also h and ϕ).

Although two new regions of significant apparent basal melting are found, $\dot{m} < 0$ for the large majority (87%) of the portion of the GrIS where we calculated this quantity, potentially suggesting widespread basal freeze-on (Figures 5a and 5d). While basal freeze-on has been inferred for several portions of the northern GrIS, including where we find $\dot{m} < 0$ [*Bell et al.*, 2014; *Wolovick et al.*, 2014], it is not anticipated to be as widespread as implied by these calculations for two reasons: (1) the model's assumption of plug flow and (2) because thermodynamic considerations and likely geothermal flux values ($\sim 55 \text{ mW m}^{-2}$ [*Shapiro and Ritzwoller*, 2004]) imply that widespread and sustained basal freeze-on at high rates ($>5 \text{ cm a}^{-1}$) is unlikely. The likely cause of the widespread inference of $\dot{m} < 0$ is that the magnitude of the mean vertical strain rate in the 9–0 ka portion of the ice column is greater than that of a Nye model where $\dot{m} = 0$. The simplest explanation for this pattern is that sufficient vertical shearing is occurring deeper within the ice column, as in a Dansgaard–Johnsen model, that the presumably low rate of basal melting or freeze-on beneath most (but not all) of the ice sheet interior cannot be well constrained by modeling of isochrones younger than 9 ka.

The pattern of h (Figures 5b and 5e and 6b–6f) shows that vertical shear within the GrIS is remarkably heterogeneous. Regions where $h < 0$ and $\dot{m} > 0$ are well correlated, as expected. *Dansgaard and Johnsen* [1969] originally developed their ice-flow model for Camp Century and estimated $h = 400 \text{ m}$ there. We find similar values in the vicinity of Camp Century but also substantially larger values farther inland and nearby (<50 km away). Variability in h is expected but has not been considered previously at this spatial scale. Following *Waddington et al.* [2005], $h \approx 0.7H$ is anticipated in the vicinity of an ice divide and $h \approx 0.25H$ is anticipated elsewhere in the interior, where the ice sheet is in “flank” flow. We find that h is often larger at ice divides, but not uniformly so, particularly in the southern GrIS. At the confluence of multiple ice divides, >100 km east of NEEM, h does approach the expected range for divide flow ($>2000 \text{ m}$ or $>0.5H$). The pattern of flank flow is variable and generally differs between adjacent IDSSs. The basal shear layer thickness tends to be larger west of the central ice divides, except in regions of apparent basal melt.

The shape factor ϕ is related directly to h (equation (3)). As such, the GrIS-wide pattern and interpretation of ϕ closely resemble that of h and \dot{m} (Figures 5c and 5f and 6g–6i). The advantage of considering ϕ over the other two 1-D modeled parameters is that interpretation of its values can constrain the location of both frozen and thawed beds, as opposed to only thawed beds. This analysis shows that the largest contiguous region of ambiguous basal thermal state is centered on the central ice divide in the southern GrIS, encompassing the uppermost reaches of IDSSs 4.1, 6.2, and 7.1. Elsewhere, the transition from an apparently frozen bed to a thawed one is often abrupt, occurring across a region of less than 50 km.

Figure 7a shows a histogram of ϕ values and conventional glaciological interpretations thereof. Where $\phi \geq 1$ indicates that basal motion is likely occurring and that the Dansgaard–Johnsen model's assumption that basal melting is negligible is no longer valid. Conversely, if we assume that $n = 1$ (a potential lower limit value at ice divides [*Pettit and Waddington*, 2003]), then where $\phi < 0.67$ ($[(n+1)/(n+2)]$) indicates that basal freeze-on is likely occurring. The gridded ϕ distribution is skewed left compared to the along-track distribution, likely because of the sparser radar coverage in regions of low along-track ϕ values (e.g., western interior). Both distributions peak above 0.67 but below 0.8 ($[(n+1)/(n+2)]$, assuming $n = 3$). Assuming that a large but unspecified portion of the GrIS interior is indeed frozen and that its flow is adequately represented by the Dansgaard–Johnsen model, this observation implies that the effective value of n for the GrIS interior is somewhat less than 3. This result is consistent with the assumed rheology embedded in most ice-flow models, including equation (6). Excluding observations near ice divides, where n is less clearly approximated by 3 [e.g., *Pettit and Waddington*, 2003; *Gillet-Chauvet et al.*, 2011], does not affect these ϕ distributions significantly.

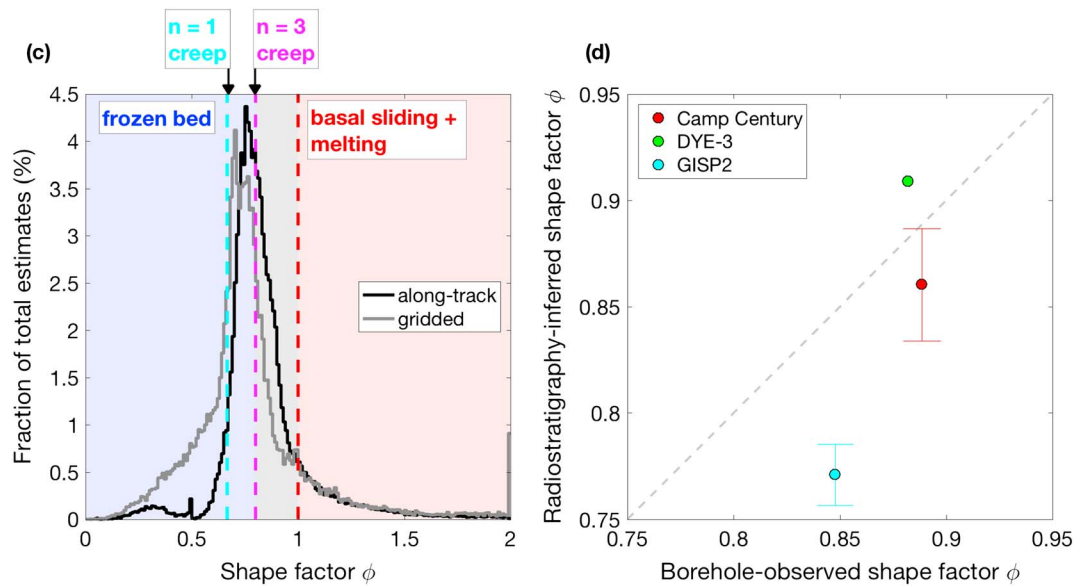


Figure 7. (a) Histogram of along-track and gridded shape factor ϕ values (Figures 5c and 5f), overlaid on the qualitative physical interpretation of ϕ values. Note that the extent of these values does not typically reach the ice sheet margin and includes ice divides. The small peak at $\phi = 0.5$ for the along-track values is an anomaly associated with the optimization method that can lead to $h = H$ (equation (5)). (b) Comparison between borehole-observed and radiostratigraphy-inferred ϕ values from radar transects that pass within 3 km of the boreholes. For boreholes with multiple radiostratigraphy-inferred estimates of ϕ , the standard deviation is also shown using error bars.

A comparison between borehole-measured ϕ values and those we infer from the radiostratigraphy (Figure 7b) shows that we tend to underestimate ϕ relative to borehole observations. This underestimation is most apparent at GISP2 (borehole: 0.85; radiostratigraphy: 0.77 ± 0.01), which is frozen at the bed. The most likely explanation for this underestimation is that ice flow was nonsteady over the period represented by the entire ice column, as opposed to that which we infer from the 9–0 ka portion of the ice column only. A nonuniform rate factor in situ may also influence this difference. Given the paucity of borehole-measured ϕ values, we cannot perform an ice sheet-wide correction to these values. Hence, while we use ϕ values to infer the basal thermal state from radiostratigraphy, we acknowledge that it may underestimate (overestimate) the portion of the bed that is thawed (frozen).

3.3. Surface Constraints on Regions of Likely Basal Motion

3.3.1. Surface Velocity

The filtered surface-velocity u_s , the temperate-column estimate of u_{def} , and the ratio of these two quantities (u_s/u_{def}) are shown in Figure 8. Lower and upper bound estimates of $u_s/u_{\text{def}} = 1$ are determined using the reported uncertainty for u_s and our modeling uncertainty for u_{def} .

Except for NEGIS and small regions along the central ice divides, where flow azimuths are not as well constrained, this analysis infers the presence of basal motion within ~50–250 km of most of the GrIS margin. This pattern is clearer away from ice divides that reach the margin, and u_s/u_{def} tends to be greater along the western margin than the eastern margin. This analysis infers basal motion at NorthGRIP, where the bed is thawed, but not at the other interior boreholes.

The along-flow uncertainty in the region where $u_s/u_{\text{def}} > 1$ generally exceeds 200 km, especially in southwestern (IDS 6.2) and northwestern Greenland (IDS 1.1 and 8.1), near radiostratigraphically identified regions of basal motion (Figures 5c and 5f). This large uncertainty is due primarily to uncertainty in ice thickness in the ice sheet interior and to a lesser extent by the assumed relative uncertainty in the rate factor for temperate ice.

3.3.2. Surface Texture

Figure 9 shows the contrast-stretched MOG and our traced outlines of the onset of surface undulations, based on both a standard and a conservative assessment of MOG surface texture. Several zoom-ins of MOG are also shown (same regions as Figure 6). Although NEGIS is a prominent feature of the surface of

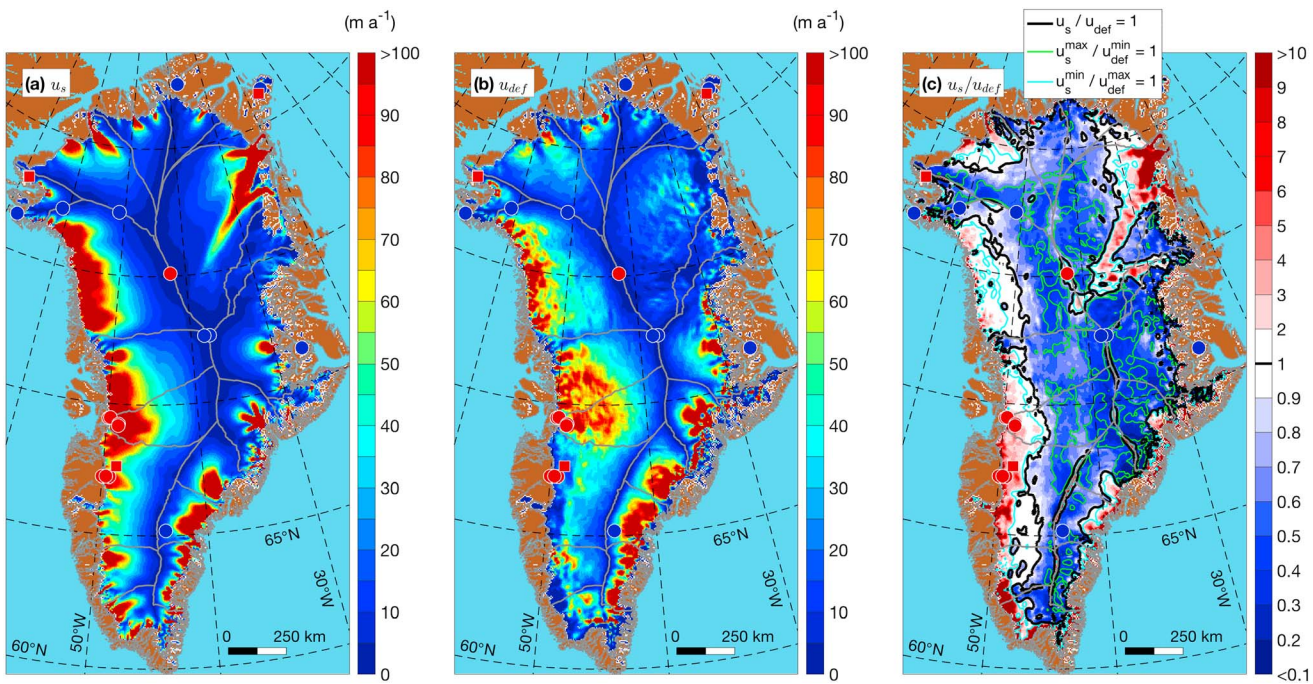


Figure 8. (a) Observed surface speed (u_s) across the GrIS [Joughin *et al.*, 2010], filtered following MacGregor *et al.* [2016]. (b) Modeled ice-deformation speed at surface (u_{def}) assuming an entirely temperate ice column ($\bar{A} = 2.4 \times 10^{-24} \text{ Pa}^{-3} \text{ s}^{-1}$; equation (6)). (c) Ratio of observed to modeled surface speed (u_s/u_{def}). Bold contours represent $u_s/u_{\text{def}} = 1$, considering both the standard values shown in Figures 8a and 8b and uncertainty in both quantities.

the GrIS and its shear margins are well defined [Fahnestock *et al.*, 1993], in terms of the onset of surface undulations, it is otherwise undistinguished compared to elsewhere on the GrIS. The central ice divide is smooth, but the deep interior of the southern GrIS is relatively rough and the onset of surface undulations reaches the ice divide below 65°N , near DYE-3. In general, the standard and conservative estimates of the surface-undulation onset agree well, except in two relatively small regions southwest of the summit region (GRIP/GISP2) and north of NEGIS.

3.4. Synthesis of Basal Thermal State Estimates

Figure 10 shows the agreement between the four estimates of the GrIS basal thermal state, along with cold- and warm-bias versions of this agreement. Only thermomechanical models can estimate where the bed is both frozen and thawed for the entire ice sheet. Analysis of ϕ can constrain the location of frozen and thawed beds but not for the entire ice sheet. Our surface-velocity and surface-imagery analyses constrain only where basal motion is likely. Hence, any synthesis of these four methods is biased toward inferring a thawed bed.

Figure 10a illustrates the variety of estimates of the frozen/thawed transition generated by the four methods. Although the large-scale structure of all these estimates broadly resembles a scalloped frozen core, the details of this structure and its total extent vary significantly. Nevertheless, in some portions of the GrIS, multiple methods agree well at small scales ($<100 \text{ km}$), e.g., the frozen/thawed transition in west-central Greenland (IDS 7.2) as estimated independently by both the 3-D models and MOG surface undulations.

Table 3 summarizes the portion of the GrIS bed that is identified as frozen or thawed by each method. The SeaRISE synthesis suggests that a greater portion of the GrIS bed is frozen (56–80%) than that inferred from radiostratigraphy (19–41%). Only 10% of the GrIS is identified as thawed from radiostratigraphy, and this range is narrow (9–12%). The surface-velocity analysis has the greatest range of inferred thawed bed (18–76%), whereas the surface-texture analysis produces the largest standard estimate of the thawed extent of the GrIS bed (69%).

For both the standard and cold-bias agreement masks (Figures 10b and 10c, respectively), the extent of the scalloped frozen core is similar. This similarity occurs because only two of the methods can constrain indirectly where the bed is frozen. The primary difference between these two masks is the extent of the uncertain

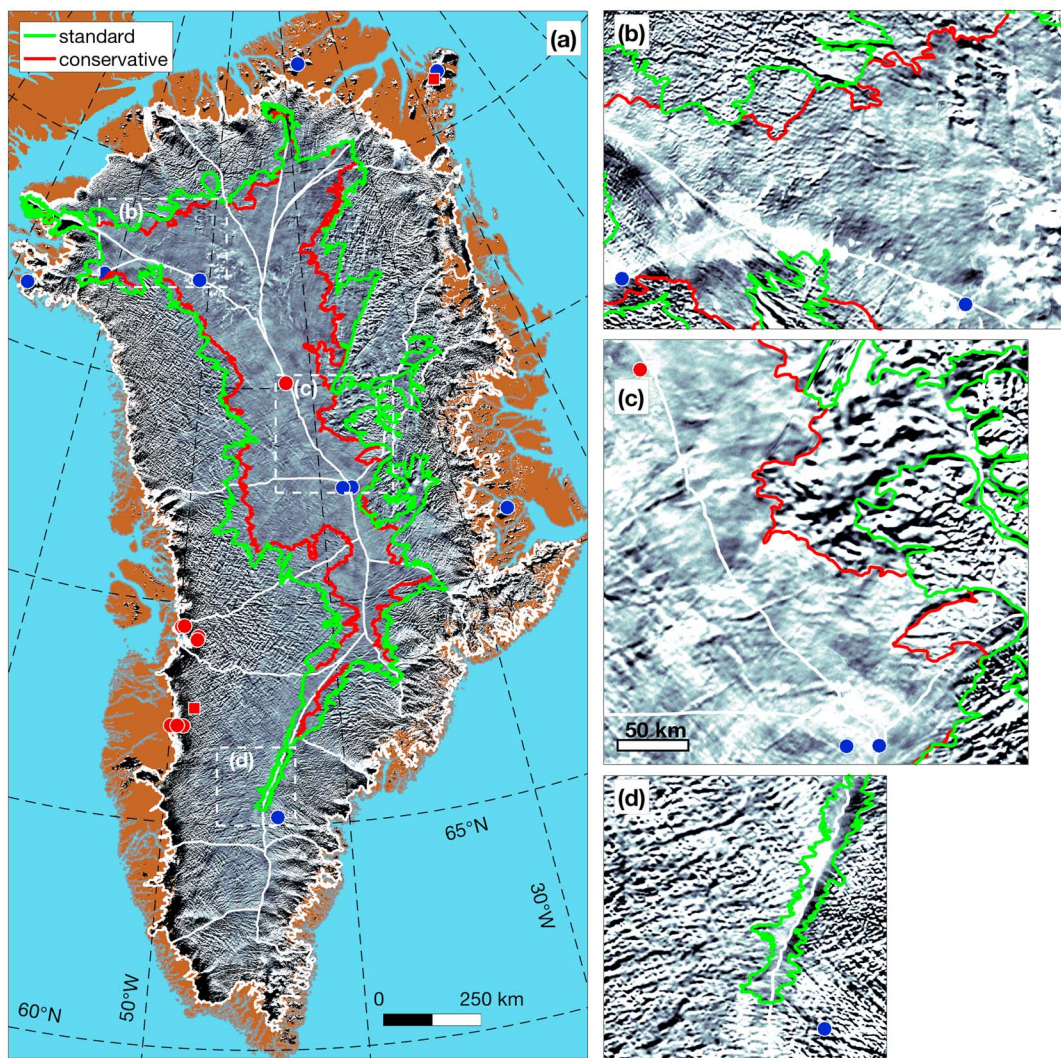


Figure 9. (a) Delineated onset of surface undulations across the GrIS. Green and red lines represent the standard and conservative estimates of the location of the onset of surface undulations, respectively. (b–d) Zoomed-in versions of the boxes identified in Figure 9a at the same scale, which is given in Figure 9c. Zoomed-in regions are the same as Figure 6.

region (no or low agreement). The warm-bias mask (Figure 10d), which has a smaller scalloped frozen core, is more distinct from the standard mask and has generally greater agreement regarding the location of a thawed bed. For all agreement masks, most interior boreholes are represented correctly as frozen. However, there is no agreement regarding NorthGRIP's basal thermal state for any mask, and in the standard and warm-bias masks it straddles the boundary between large regions of agreement that bed is frozen (to the west of NorthGRIP) and thawed (to the east). Further, for all agreement masks, DYE-3 is identified as thawed, rather than frozen.

Figure 11 shows the likely basal thermal state of the GrIS, based on the above agreement and its confidence bounds. We find that 43% of the bed is likely thawed, 24% is likely frozen, and the thermal state of the remainder (34%) is uncertain (Table 3). The hole-filling operation adjusts the size of these regions by less than 0.5% each. The distribution of each region amalgamates many of the characteristics described above. (1) The largest contiguous regions of likely thawed bed are in southwestern Greenland (primarily IDS 6.1, 6.2, and 7.1), along the northwestern coast (IDS 8.1) and within the NEGIS system (IDS 2.1), especially NEGIS itself. (2) The portion of the GrIS bed that is likely frozen lies between 68°N and 80°N and is generally west of the central ice divides. (3) Smaller discontinuous marginal regions associated with major outlet glaciers are likely thawed (e.g., Helheim Glacier in IDS 4.1 and Humboldt and Petermann Glaciers in IDS 1.1). (4) The thermal state of

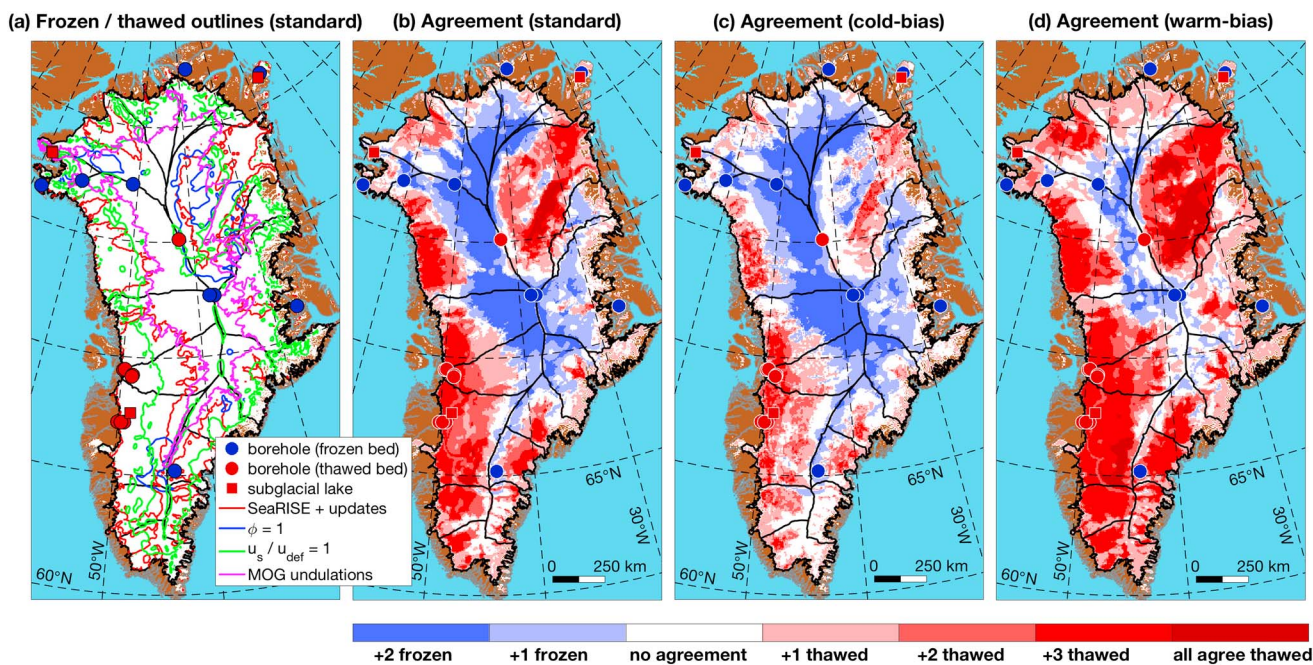


Figure 10. (a) Outlines of boundaries between a frozen and thawed GrIS bed for the four methods considered in this study (sections 2.1–2.3; Figures 4, 5f, 8c, and 9). For the 3-D models, the outline of their agreement denotes where more than half of the SeaRISE models agree that the bed is thawed, based on their synthesis (Figure 4). (b) Agreement between the four methods (S) regarding the basal thermal state. (c) Cold- and warm-bias agreement (S_{cold} and S_{warm} , respectively) determined using each method's confidence bounds or uncertainty estimates. Because only two applied methods constrain where the bed is frozen (3-D models and ϕ), but all four constrain where it is thawed, the range of S is +2 frozen to +4 (all) thawed.

the bed is uncertain within large contiguous swaths of the GrIS interior that can be >100 km wide along-flow. (5) The majority of the ablation zone is identified as likely thawed (65%), and none of it is likely frozen.

Figure 12 shows the relationships between the likely basal thermal state and several fundamental ice sheet properties. While the uncertain region complicates interpretation of these relationships and no property provides an unambiguous binary distinction between a frozen and a thawed bed, some noteworthy patterns emerge. Both increasing surface elevation and ice thickness result in a greater likelihood of a frozen bed, while increasing surface slope and speed imply that a thawed bed is more likely. Surface elevation and ice thickness covary, so the consistency of their relationships is unsurprising, as is the relationship between likely basal thermal state and surface speed. Above a surface slope of 50 m km^{-1} or speed of 100 m a^{-1} , a frozen bed is unlikely. While driving stress is related to both surface slope and ice thickness, either thermal state is possible across the range of inferred values. For example, between 30 and 70 kPa, a frozen bed is more likely, but for values outside of this range a thawed bed is more likely. A similar pattern occurs for modeled surface mass balance, but its distribution is more complex. Between 15 and 30 cm a^{-1} , a frozen bed is more than twice as likely as a thawed bed, but below 10 cm a^{-1} , a thawed bed is most likely.

Table 3. Areal Fraction of Inferred Basal Thermal State of the GrIS by Method and Synthesis

Method	Basal Thermal State (%) ^a		
	Frozen	Thawed	Uncertain
3-D thermomechanical model	63 (56–80)	29 (10–37)	8 (7–10)
Shape factor from radiostratigraphy	40 (19–41)	10 (9–12)	14 (14–32)
Maximum deformation speed	N/A	33 (18–76)	N/A
Surface texture ^b	N/A	69 (N/A–78)	N/A
Synthesis ^b	24	43	34

^aStandard value followed by range in parentheses. Values rounded to integer percentage.

^bLikely basal thermal state as shown in Figure 11 and following hole-filling operation.

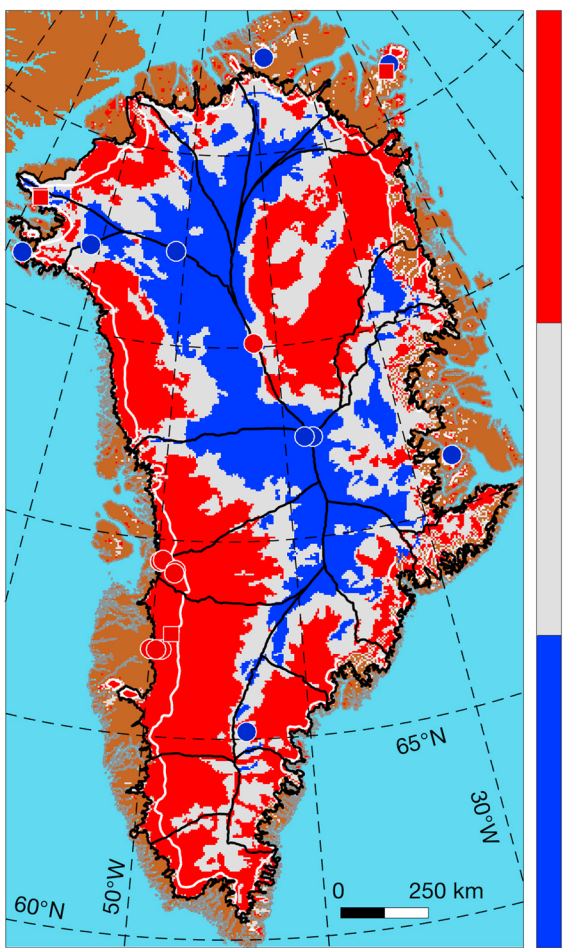


Figure 11. Likely basal thermal state of the GrIS (L), based on where the standard, cold- and warm-bias estimates of this state agree (Figures 10b–10d, section 2.4, and Table 3). The white line represents where the 1979–2014 mean surface mass balance is zero, i.e., the approximate equilibrium line, as modeled by the Modèle Atmosphérique Régionale (MAR v3.5.2) [Fettweis, 2007].

Rogozhina et al., 2016]. Confidence regarding a frozen bed is restricted mostly to the vicinity of boreholes and a contiguous region in northern and central Greenland.

To date, the majority of boreholes drilled through the GrIS are located where our synthesis suggests that the thermal state of the bed is reasonably well constrained (Figure 11). That argument is somewhat circular, because some of the 3-D thermomechanical models were tuned to match contemporary borehole observations. Only NorthGRIP and DYE-3 are located within regions that remain poorly constrained. The standard hypothesis explaining these discrepancies is that an incorrect geothermal flux in these regions leads to an incorrectly predicted basal thermal state, a problem that can be addressed by adjusting the geothermal flux [e.g., Greve, 2005; Seroussi et al., 2013; Rogozhina et al., 2016]. While certainly plausible, this hypothesis can be invoked only for the 3-D thermomechanical models, which directly apply the geothermal flux as a boundary condition, and not for the other three methods included in our synthesis. Yet those other methods also produced varied responses in the vicinity of these two boreholes. This pattern suggests that the underlying cause of the NorthGRIP/DYE-3 discrepancy stems from more than just poorly known geothermal flux and that some other property or process must also be invoked (e.g., spatially varying basal friction or rheology). Within ~200 km of NorthGRIP, this extended hypothesis is qualitatively consistent with the results of Christianson et al. [2014]. They reported observations of dilatant till within NEGIS but not outside of it, emphasizing the likelihood of spatially variable basal properties within the NEGIS drainage system.

4. Discussion

For ice sheet-wide applications, no single method considered here determines the thermal state of the bed of the ice sheet in a manner that is clearly more reliable than all others. The 3-D thermomechanical models include more complex physical representations and more boundary conditions, but not all physical processes or boundary conditions are yet sufficiently well understood. Further, there is a commensurate increase in the challenge of interpreting results from such models. Our synthesis (Figures 10 and 11) demonstrates that significant uncertainty remains in the present basal thermal state of the GrIS, even with respect to ice sheet properties that are often considered diagnostic (e.g., surface velocity; Figure 12). This uncertainty must be considered when evaluating processes that rely substantially on that state [e.g., Colgan et al., 2015]. In certain regions (e.g., southwestern Greenland, NEGIS, the onset regions of major outlet glaciers), we can be reasonably confident that the bed is thawed contiguously at the scales considered here (≥ 5 km), supporting the conclusions of earlier studies related to those regions [e.g., Fahnestock et al., 2001; Poinar et al., 2015; Tedstone et al., 2015];

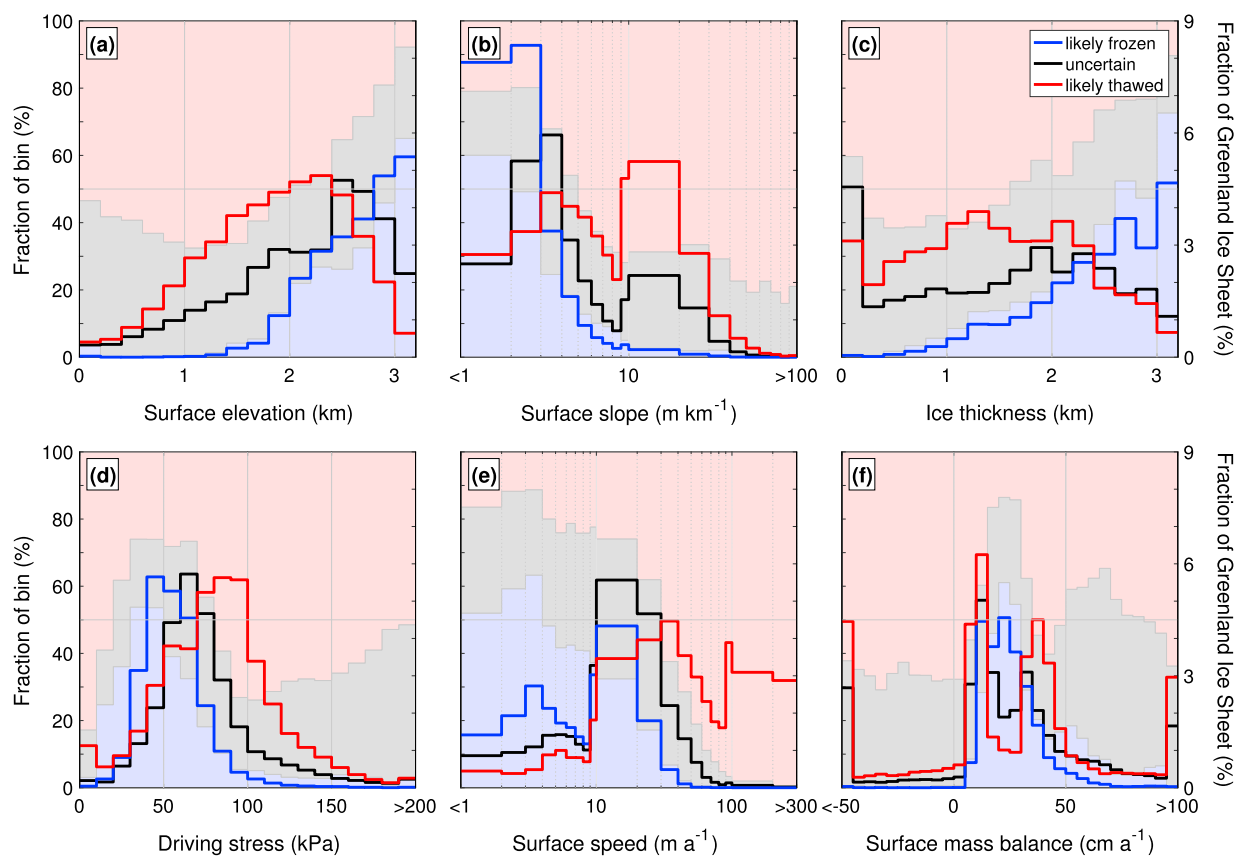


Figure 12. (right y axis; lines) Areal distributions of readily observed or inferred GrIS properties as a function of likely basal thermal state (L ; Figure 11). (left y axis; background fill) Relative fraction of the three possible values of L (likely frozen, uncertain, or likely thawed) contained within each bin. (a) Surface elevation and (b) slope are derived from GIMP [Howat et al., 2014], (c) ice thickness from Morlighem et al. [2014], (d) driving stress from Figure 1b, (e) surface speed from Figure 8a, and (f) surface mass balance from MAR (same as in Figure 11).

Our synthesis evinces a pattern in northeastern Greenland that may have wider implications for our understanding of GrIS thermodynamics. The transition between a likely frozen bed and an uncertain basal thermal state follows the western and northern boundaries of the NEGIS system (its interior ice divide) remarkably well (IDS 2.1; Figure 11). Both 3-D models and radiostratigraphic analysis agree regarding the large-scale structure of this transition, if not its exact position (Figure 10). There is also a large gradient in the Holocene-averaged accumulation rate across this ice divide [MacGregor et al., 2016], suggesting a strong coupling there between local accumulation rate and basal thermal state. Such a coupling could have arisen in at least two ways. First, ice in this region flows slowly ($<10 \text{ m a}^{-1}$; Figure 8a), so if this region has been quasi-stable for tens of millennia, temperature-depth profiles may be approximated using a 1-D steady state model [Cuffey and Paterson, 2010]. For a given geothermal flux and surface temperature, such models predict that a lower accumulation rate results in a greater likelihood of a thawed bed. Second, a heretofore-unrecognized boundary in Greenland's subglacial geology could exist at or near this ice divide [Dawes, 2009; Rogozhina et al., 2016]. This boundary could influence the local basal thermal state through a horizontal gradient in the geothermal flux, potentially leading to basal motion within the NEGIS system and ice drawdown, thus influencing the present position of the ice divide as determined from surface topography [Zwally et al., 2012].

The large region of uncertain basal thermal state also indirectly informs our understanding of ice sheet thermodynamics. Undoubtedly, part of the extent of the uncertain region is due to artifacts or limitations in our methodology and synthesis. Nevertheless, our synthesis suggests that the basal thermal state typically transitions from frozen to thawed over a relatively wide region (often $>100 \text{ km}$ along-flow). The along-flow width of this uncertain region represents the distance over which ice must flow before its modeled state, englacial, and surface properties consistently indicate a thawed bed. Such a transition likely exhibits large spatiotemporal variability that is only partly tied to local basal properties, in particular the geothermal flux

[*van der Veen et al.*, 2007; *Brinkerhoff et al.*, 2011; *Meierbachtol et al.*, 2015], and can also be influenced by model resolution in some regions [*Aschwanden et al.*, 2016]. Heat advection (whether englacial or subglacial) and dynamic thinning or thickening can modify the local basal temperature gradient significantly at centennial time scales. In turn, the frozen/thawed boundary migrates. Such processes may be rate limited and possess negative feedback [e.g., *Huybrechts*, 1996; *Phillips et al.*, 2013; *Wolovick et al.*, 2014]. Regardless of the specific factors and history that have led to the present GrIS basal thermal state, our synthesis emphasizes that the frozen/thawed transition is unlikely to be a singular, stationary, contiguous line around the ice sheet.

Evaluations of the role of the subglacial hydrologic system in the connection between surface melting and seasonal acceleration often hinge on the assumption that the bed is thawed, as is consistently observed by boreholes in the ablation zone and supported by our synthesis (Figure 11). However, virtually, all such field studies for the GrIS have so far taken place in southwestern Greenland (IDS 6.1, 7.1, and 7.2; Table 1), within the largest contiguous thawed region of the bed. Many ground-based, remote-sensing, and modeling studies also focus on this region [e.g., *Price et al.*, 2008; *Andrews et al.*, 2014; *Poinar et al.*, 2015; *Tedstone et al.*, 2015] or other extensively thawed regions, such as the NEGIS system [*Karlsson and Dahl-Jensen*, 2015]. While recent perturbations to local subglacial hydrology may be significant along the margin there [*van de Wal et al.*, 2008], a previously unrecognized bias may be introduced by applying process-level insights from this particular region to the whole of the GrIS [e.g., *Shannon et al.*, 2013; *Tedstone et al.*, 2015]. Elsewhere along the margin of the GrIS, the bed is less clearly thawed and rarely over such a large portion of an IDS. If the upstream portion of a given IDS is not thawed, then the subglacial water contribution of that upstream region is likely much smaller than in the southwestern GrIS. This contribution likely influences the onset and evolution of efficient/channelized subglacial drainage during the summer melt season. Hence, the seasonal evolution of subglacial hydrology elsewhere along the GrIS margin could differ substantially from that directly observed and modeled so far. Identification of presently frozen regions that are experiencing new surface melting or surface-to-bed connections will help bound the impact of this process on the evolution of the basal thermal state [e.g., *Poinar et al.*, 2015; *Willis et al.*, 2015].

MacGregor et al. [2015b] inferred that most of the southern GrIS, including the SW region noted in this study, contains ice at middepths that is significantly colder than at the surface, a pattern that could not be fully explained by horizontal advection of colder inland ice. This pattern may suggest the presence of widespread basal melting that is sufficient to draw down (vertically advect) colder ice, but this possibility was discounted in favor of changing surface boundary conditions in the past (temperature and accumulation rate). Here through our synthesis, we identify a portion of this region as likely thawed, but it is not yet clear that basal melting there is fast enough to invalidate the original hypothesis regarding the cause of relatively cold ice there.

Radar bed reflectivity is commonly used to infer ice sheet basal conditions, but we did not independently evaluate or include this metric in our synthesis due to the challenge of calibrating bed reflectivity across an entire ice sheet. *Oswald and Gogineni* [2012] undertook the most extensive investigation of GrIS bed reflectivity so far, but their analysis was focused on the northern half of the GrIS only. Several regions and at least one borehole that they identified as possessing a wet bed are identified as either likely frozen or uncertain by our synthesis and existing borehole measurements (IDS 1.1, 1.2, and 8.2; Camp Century), but there appears to be better agreement regarding a thawed bed within the NEGIS system (IDS 2.1) [*Rogozhina et al.*, 2016]. Further analysis of existing extensive radar data is clearly necessary to reconcile these differences, perhaps by applying existing methods to newer data [e.g., *Oswald and Gogineni*, 2008, 2012; *Christianson et al.*, 2014] or newer methods to existing data [e.g., *Schroeder et al.*, 2013, 2014, 2016; *MacGregor et al.*, 2015b].

Using a suite of 3-D thermomechanical model runs, *Pattyn* [2010] predicted that ~55% of the grounded Antarctic Ice Sheet are thawed at its bed, a value somewhat larger than the 43% we report here for the GrIS. Given the size of the uncertain region we identify (34%), these total values cannot be considered to be significantly different, but it is worthwhile to consider the difference between our synthesis of the GrIS's likely basal thermal state (Figure 11) and that reported by *Pattyn* [2010] for Antarctica. The GrIS pattern generally transitions along-flow from frozen to uncertain to thawed, whereas for Antarctica this pattern is often reversed, most notably in East Antarctica. This pattern is presumably due to the generally larger ice thicknesses and lower accumulation rates in East Antarctica as compared to Greenland (Figure 12). *Pattyn* [2010] only considered 3-D models in his assessment, while we synthesized multiple independent methods. However, our synthesis of GrIS 3-D models (Figure 4) more closely resembles our final synthesis than the other

methods (Figure 11), supporting the notion that evaluation of either multiple distinct models or multiple instances of a single model are prudent paths when seeking to constrain the basal thermal state of an ice sheet.

5. Conclusions

We evaluated the present basal thermal state of the GrIS using four independent methods: 3-D thermomechanical modeling and basal motion inferred from radiostratigraphy, surface velocity, and surface texture, respectively. These methods vary in their degree of sophistication, but all are motivated by their ability to potentially discriminate between frozen and thawed beds. The resulting synthesis identifies distinct regions, where the bed is likely frozen (24% by area) or thawed (43%) and where this basal thermal state remains most uncertain (34%).

This first synthesis of the location of the ice sheet's scalloped frozen core and thawed margins, along with the substantial region of uncertain basal thermal state, are a fundamental constraint on the ice sheet's large-scale thermodynamics. We find that the three largest regions of the ice sheet that are likely contiguously thawed are the southwest margin, the northwest margin, and NEGIS (both the trunk and coastal mouth). A frozen bed is likely west of the central ice divides and in the summit region.

Future work to constrain the basal thermal state of the GrIS should focus on the region that we identify as most uncertain. This region is mostly away from present ice divides, where the ice sheet is in flank flow. It is also where additional borehole measurements to the bed and remote observations would most improve our understanding of the basal thermal state of the GrIS. Such measurements concern not only the basal temperature itself but also the geothermal flux, as inferred from the vertical basal temperature gradients within the ice and underlying rock [e.g., Cuffey *et al.*, 1995; Fisher *et al.*, 2015; Rogozhina *et al.*, 2016]. Improved knowledge of the relatively stable geothermal flux is at least as valuable for predictive ice sheet modeling as knowledge of the present basal temperature and its vertical gradient, although the latter two quantities are more easily compared with observations.

Acknowledgments

NSF (ARC 1107753 and 1108058 and ANT 0424589) and NASA (NNX12AB71G, NNX13AM16G, NNX13AK27G, and NNX13AD53A) supported this work. We thank the organizations (Program for Arctic Regional Climate Assessment, Center for Remote Sensing of Ice Sheets, Operation IceBridge, and SeaRISE) and innumerable individuals that both supported and performed the development, collection, and processing of the radar data and numerical models used in this study. G.D. Clow was supported by the U.S. Geological Survey Climate and Land Use Change Program. S.F. Price was supported by the U.S. Department of Energy Office of Science's Biological and Environmental Research Program. H. Seroussi was supported by NASA Cryospheric Sciences and Modeling Analysis and Prediction Programs, under a contract with Caltech's Jet Propulsion Laboratory. We thank A.N. Mabrey for analyzing the MOG surface texture, I. Joughin for providing the updated composite surface-velocity field, H. Thomsen for the borehole-temperature data, and L.C. Andrews for the valuable discussions. We thank the Editor, Associate Editor, M. Lüthi, and two anonymous reviews for their constructive reviews that substantially improved this manuscript. A mask of the likely basal thermal state of the GrIS (Figure 11) will be archived at the National Snow and Ice Data Center.

References

- Alley, R. B., P. U. Clark, P. Huybrechts, and I. Joughin (2005), Ice-sheet and sea-level changes, *Science*, **310**, 456–460.
- Andrews, L. C., G. A. Catania, M. J. Hoffman, J. D. Gulley, M. P. Lüthi, C. Ryser, R. L. Hawley, and T. A. Neumann (2014), Direct observations of evolving subglacial drainage beneath the Greenland Ice Sheet, *Nature*, **514**, 80–83, doi:10.1038/nature13796.
- Aschwanden, A., E. Bueler, C. Khroulev, and H. Blatter (2012), An enthalpy formulation for glaciers and ice sheets, *J. Glaciol.*, **58**(209), 441–457, doi:10.3189/2012JoG11J088.
- Aschwanden, A., G. Aðalgeirsdóttir, and C. Khroulev (2013), Hindcasting to measure ice sheet model sensitivity to initial states, *Cryosphere*, **7**, 1083–1093, doi:10.5194/tc-7-1083-2013.
- Aschwanden, A., M. A. Fahnestock, and M. Truffer (2016), Complex Greenland outlet glacier flow captured, *Nat. Commun.*, **7**, 10524, doi:10.1038/ncomms10524.
- Bell, R. E., M. Studinger, C. A. Shuman, M. A. Fahnestock, and I. Joughin (2007), Large subglacial lakes in East Antarctica at the onset of fast-flowing ice streams, *Nature*, **445**(7130), 904–907, doi:10.1038/nature05554.
- Bell, R. E., K. Tinto, I. Das, M. Wolovick, W. Chu, T. T. Creyts, N. Frearson, A. Abdi, and J. D. Paden (2014), Deformation, warming and softening of Greenland's ice by refreezing meltwater, *Nat. Geosci.*, **7**, 497–502, doi:10.1038/ngeo2179.
- Bender, M. L., E. Burgess, R. B. Alley, B. Barnett, and G. D. Clow (2010), On the nature of dirty ice at the bottom of the GISP2 ice core, *Earth Planet. Sci. Lett.*, **299**, 466–473, doi:10.1016/j.epsl.2010.09.033.
- Brinkerhoff, D. J., and J. V. Johnson (2013), Data assimilation and prognostic whole ice sheet modelling with the variationally derived, higher order, open source, and fully parallel ice sheet model VarGlaS, *Cryosphere*, **7**, 1161–1184, doi:10.5194/tc-7-1161-2013.
- Brinkerhoff, D. J., T. W. Meierbachtol, J. V. Johnson, and J. T. Harper (2011), Sensitivity of the frozen/melted basal boundary condition to perturbations of basal traction and geothermal heat flux: Isunngua Sermia, western Greenland, *Ann. Glaciol.*, **52**(59), 43–50.
- Calov, R., and K. Hutter (1996), The thermomechanical response of the Greenland Ice Sheet to various climate scenarios, *Clim. Dyn.*, **12**, 243–260.
- Christianson, K., L. E. Peters, R. B. Alley, S. Anandakrishnan, R. W. Jacobel, K. L. Riverman, A. Muto, and B. A. Keisling (2014), Dilatant till facilitates ice-stream flow in northeast Greenland, *Earth Planet. Sci. Lett.*, **401**, 57–69, doi:10.1016/j.epsl.2014.05.060.
- Colgan, W., A. Sommers, H. Rajaram, W. Abdalati, and J. Fahrm (2015), Considering thermal-viscous collapse of the Greenland Ice Sheet, *Earth's Future*, **3**, 252–267, doi:10.1002/2015EF000301.
- Cuffey, K. M., and W. S. B. Paterson (2010), *The Physics of Glaciers*, 4th ed., 693 pp., Butterworth-Heinemann, Burlington, Mass.
- Cuffey, K. M., G. D. Clow, R. B. Alley, M. Stuiver, E. D. Waddington, and R. W. Saltus (1995), Large Arctic temperature change at the Wisconsin-Holocene glacial transition, *Science*, **270**, 455–458.
- Dahl-Jensen, D., and N. S. Gundestrup (1987), Constitutive properties of ice at Dye 3, Greenland, in *In The Physical Basis of Ice Sheet Modelling*, IAHS Publ., vol. 70, edited by E. D. Waddington and J. S. Walder, pp. 31–43, Oxford, U. K.
- Dahl-Jensen, D., N. S. Gundestrup, K. Keller, S. J. Johnsen, S. P. Gogineni, C. T. Allen, T. S. Chuah, H. Miller, S. Kipfstuhl, and E. D. Waddington (1997), A search in north Greenland for a new ice-core drill site, *J. Glaciol.*, **43**(144), 300–306.
- Dahl-Jensen, D., K. Mosegaard, N. Gundestrup, G. D. Clow, S. J. Johnsen, A. W. Hansen, and N. Balling (1998), Past temperatures directly from the Greenland Ice Sheet, *Science*, **282**(5387), 268–271.

- Dahl-Jensen, D., N. Gundestrup, S. P. Gogineni, and H. Miller (2003), Basal melt at NorthGRIP modeled from borehole, ice-core and radio-echo sounder observations, *Ann. Glaciol.*, 37, 207–212.
- Dansgaard, W., and S. J. Johnsen (1969), A flow model and a time scale for the ice core from Camp Century, Greenland, *J. Glaciol.*, 8(53), 215–223.
- Dawes, P. R. (2009), The bedrock geology under the Inland Ice: The next major challenge for Greenland mapping, *Geol. Surv. Greenl. Den. Bull.*, 17, 57–60.
- De Rydt, J., G. H. Gudmundsson, H. F. J. Corr, and P. Christoffersen (2013), Surface undulations of Antarctic ice streams tightly controlled by bedrock topography, *Cryosphere*, 7, 407–417, doi:10.5194/tc-7-407-2013.
- Dukowicz, J. K., S. F. Price, and W. H. Lipscomb (2010), Consistent approximations and boundary conditions for ice-sheet dynamics from a principle of least action, *J. Glaciol.*, 56(197), 480–496.
- Fahnestock, M., R. Bindschadler, R. Kwok, and K. Jezek (1993), Greenland Ice Sheet surface properties and ice dynamics from ERS-1 SAR imagery, *Science*, 262, 1530–1534.
- Fahnestock, M., W. Abdalati, I. Joughin, J. Brozena, and P. Gogineni (2001), High geothermal heat flow, basal melt, and the origin of the rapid ice flow in central Greenland, *Science*, 294(5550), 2338–2342.
- Fettweis, X. (2007), Reconstruction of the 1979–2006 Greenland Ice Sheet surface mass balance using the regional climate model MAR, *Cryosphere*, 1, 21–40, doi:10.5194/tc-1-21-2007.
- Fisher, A. T., K. D. Mankoff, S. M. Tulaczyk, S. W. Tyler, N. Foley, and WISSARD Science Team (2015), High geothermal heat flux measured below the West Antarctic Ice Sheet, *Sci. Adv.*, 1, e1500093, doi:10.1126/sciadv.1500093.
- Funk, M., K. Echelmeyer, and A. Iken (1994), Mechanisms of fast flow in Jakobshavn Isbræ, West Greenland: Part II. Modeling of englacial temperatures, *J. Glaciol.*, 40(136), 569–585.
- Gillet-Chauvet, F., R. C. A. Hindmarsh, H. F. J. Corr, E. C. King, and A. Jenkins (2011), In-situ quantification of ice rheology and direct measurement of the Raymond Effect at Summit, Greenland using a phase-sensitive radar, *Geophys. Res. Lett.*, 38, L24503, doi:10.1029/2011GL049843.
- Greve, R. (1997), Application of a polythermal three-dimensional ice sheet model to the Greenland Ice Sheet: Response to steady-state and transient climate scenarios, *J. Clim.*, 10(5), 901–918.
- Greve, R. (2005), Relation of measured basal temperatures and the spatial distribution of the geothermal heat flux for the Greenland Ice Sheet, *Ann. Glaciol.*, 42, 424–432.
- Greve, R., and K. Hutter (1995), Polythermal three-dimensional modelling of the Greenland Ice Sheet with varied geothermal flux, *Ann. Glaciol.*, 21, 8–12.
- Gudmundsson, G. H. (2003), Transmission of basal variability to a glacier surface, *J. Geophys. Res.*, 108(B5), 2253, doi:10.1029/2002JB002107.
- Gundestrup, N., and B. L. Hansen (1984), Bore-hole survey at DYE 3, South Greenland, *J. Glaciol.*, 30(106), 282–288.
- Gundestrup, N., D. Dahl-Jensen, B. L. Hansen, and J. Kelty (1993), Bore-hole survey at Camp Century, 1989, *Cold Reg. Sci. Technol.*, 21, 187–193.
- Hansson, M. E. (1994), The Renland ice core. A Northern Hemisphere record of aerosol composition over 120,000 years, *Tellus, Ser. B*, 46, 390–418.
- Haran, T., J. Bohlander, T. Scambos, T. Painter, and M. Fahnestock (2013), MEaSUREs MODIS Mosaic of Greenland 2005 (MOG2005) image map, Version 1, Natl. Snow Ice Data Cent., Boulder, Colo., doi:10.5067/LAGYM8Q26QRE.
- Harrington, J. A., N. F. Humphrey, and J. T. Harper (2015), Temperature distribution and thermal anomalies along a flowline of the Greenland Ice Sheet, *Ann. Glaciol.*, 56(70), 98–104, doi:10.3189/2015AoG70A945.
- Heimbach, P., and V. Bugnion (2009), Greenland ice-sheet volume sensitivity to basal, surface and initial conditions derived from an adjoint model, *Ann. Glaciol.*, 50(52), 67–80.
- Hindmarsh, R. C. A., G. J. M. C. Leysinger Vieli, M. J. Raymond, and G. H. Gudmundsson (2006), Draping or overriding: The effect of horizontal stress gradients on internal layer architecture in ice sheets, *J. Geophys. Res.*, 111, F02018, doi:10.1029/2005JF000309.
- Howat, I. J., C. Porter, M. J. Noh, B. E. Smith, and S. Jeong (2015), Brief communication: Sudden drainage of a subglacial lake beneath the Greenland Ice Sheet, *Cryosphere*, 9, 103–108, doi:10.5194/tc-9-103-2015.
- Howat, I. M., A. Negrete, and B. E. Smith (2014), The Greenland Ice Mapping Project (GIMP) land classification and surface elevation data sets, *Cryosphere*, 8, 1509–1518, doi:10.5194/tc-8-1509-2014.
- Huylebroeck, P. (1994), The present evolution of the Greenland Ice Sheet: An assessment by modeling, *Global Planet. Change*, 9, 39–51.
- Huylebroeck, P. (1996), Basal temperature conditions of the Greenland Ice Sheet during the glacial cycles, *Ann. Glaciol.*, 23, 226–236.
- Iken, A., K. Echelmeyer, W. Harrison, and M. Funk (1993), Mechanism of fast flow in Jakobshavn Isbræ, West Greenland: Part I. Measurements of temperature and water level in boreholes, *J. Glaciol.*, 39(131), 15–25.
- Jensen, D. (1977), A three-dimensional polar ice-sheet model, *J. Glaciol.*, 18(80), 373–389.
- Joughin, I., B. E. Smith, I. M. Howat, T. Scambos, and T. Moon (2010), Greenland flow variability from ice-sheet-wide velocity mapping, *J. Glaciol.*, 56(197), 415–430.
- Karlsson, N. B., and D. Dahl-Jensen (2015), Response of the large-scale subglacial drainage system of Northeast Greenland to surface elevation changes, *Cryosphere*, 9, 1465–1479, doi:10.5194/tc-9-1465-2015.
- Keisling, B. A., K. Christianson, R. B. Alley, L. E. Peters, J. E. M. Christian, S. Anandakrishnan, K. L. Riverman, A. Muto, and R. W. Jacobel (2014), Basal conditions and ice dynamics inferred from radar-derived internal stratigraphy of the Northeast Greenland Ice Stream, *Ann. Glaciol.*, 55(67), 127–137, doi:10.3189/2014AoG67A090.
- Koutnik, M. R., T. J. Fudge, H. Conway, E. D. Waddington, T. A. Neumann, K. M. Cuffey, C. Buizert, and K. C. Taylor (2016), Holocene accumulation and ice flow near the West Antarctic Ice Sheet Divide ice core site, *J. Geophys. Res. Earth Surf.*, 121, 907–924, doi:10.1002/2015JF003668.
- Lemark, A. (2010), A study of the Flade Isblink ice cap using a simple ice flow model, M.Sc. thesis, Univ. Copenhagen.
- Lüthi, M. P., M. Funk, A. Iken, S. Gogineni, and M. Truffer (2002), Mechanisms of fast flow in Jakobshavn Isbræ, West Greenland: Part III. Measurements of ice deformation, temperature and cross-borehole conductivity in boreholes to the bedrock, *J. Glaciol.*, 48(162), 369–385.
- Lüthi, M. P., C. Ryser, L. C. Andrews, G. A. Catania, M. Funk, R. L. Hawley, M. J. Hoffman, and T. A. Neumann (2015), Heat sources within the Greenland Ice Sheet: Dissipation, temperate paleo-firn and cryo-hydrologic warming, *Cryosphere*, 9, 245–253, doi:10.5194/tc-9-245-2015.
- MacGregor, J. A., M. A. Fahnestock, G. A. Catania, J. D. Paden, S. Prasad Gogineni, S. K. Young, S. C. Rybarski, A. N. Mabrey, B. M. Wagman, and M. Morlighem (2015a), Radiostratigraphy and age structure of the Greenland Ice Sheet, *J. Geophys. Res. Earth Surf.*, 120, 212–241, doi:10.1002/2014JF003215.
- MacGregor, J. A., et al. (2015b), Radar attenuation and temperature within the Greenland Ice Sheet, *J. Geophys. Res. Earth Surf.*, 120, 983–1008, doi:10.1002/2014JF003418.
- MacGregor, J. A., W. T. Colgan, M. A. Fahnestock, M. Morlighem, G. A. Catania, J. D. Paden, and S. Prasad Gogineni (2016), Holocene deceleration of the Greenland Ice Sheet, *Science*, 351(6273), 590–593.

- Madsen, K. N., and T. Thorsteinsson (2001), Textures, fabrics and meltlayer stratigraphy in the Hans Tausen ice core, North Greenland—Indications of late Holocene ice cap generation? *Medd. Grønl. Geosci.*, 39, 97–114.
- Marshall, S. J. (2005), Recent advances in understanding ice sheet dynamics, *Earth Planet. Sci. Lett.*, 240(2), 191–204, doi:10.1016/j.epsl.2005.08.016.
- Meierbach et al. (2015), Thermal boundary conditions on western Greenland: Observational constraints and impacts on the modeled thermomechanical state, *J. Geophys. Res. Earth Surf.*, 120, 623–636, doi:10.1002/2014JF003375.
- Moon, T., I. Joughin, B. Smith, M. R. van den Broeke, W. J. van de Berg, B. Noël, and M. Usher (2014), Distinct patterns of seasonal Greenland glacier velocity, *Geophys. Res. Lett.*, 41, 7209–7216, doi:10.1002/2014GL061836.
- Morlighem, M., E. Rignot, J. Mouginot, H. Seroussi, and E. Larour (2014), Deeply incised submarine glacial valleys beneath the Greenland Ice Sheet, *Nat. Geosci.*, 7, 418–422, doi:10.1038/ngeo2167.
- Nowicki, S., et al. (2013), Insights into spatial sensitivities of ice mass response to environmental change from the SeaRISE ice sheet modeling project II: Greenland, *J. Geophys. Res. Earth Surf.*, 118, 1025–1044, doi:10.1002/jgrf.20076.
- Oswald, G. K. A., and S. P. Gogineni (2008), Recovery of subglacial water extent from Greenland radar survey data, *J. Glaciol.*, 54(184), 94–106.
- Oswald, G. K. A., and S. P. Gogineni (2012), Mapping basal melt under the northern Greenland Ice Sheet, *IEEE Trans. Geosci. Remote Sens.*, 50(2), 585–592, doi:10.1109/TGRS.2011.2162072.
- Palmer, S. J., J. A. Dowdeswell, P. Christoffersen, D. A. Young, D. D. Blankenship, J. S. Greenbaum, T. Benham, J. Bamber, and M. J. Siegert (2013), Greenland subglacial lakes detected by radar, *Geophys. Res. Lett.*, 40, 6154–6159, doi:10.1002/2013GL058383.
- Paterson, W. S. B. (1991), Why ice-age ice is sometimes “soft”, *Cold Reg. Sci. Technol.*, 20, 75–98.
- Pattyn, F. (2010), Antarctic subglacial conditions inferred from a hybrid ice sheet/ice stream model, *Earth Planet. Sci. Lett.*, 295, 451–461, doi:10.1016/j.epsl.2010.04.025.
- Petrunin, A. G., I. Rogozhina, A. P. M. Vaughan, I. T. Kukkonen, M. K. Kaban, I. Koulakov, and M. Thomas (2013), Heat flux variations beneath central Greenland’s ice due to anomalously thin lithosphere, *Nat. Geosci.*, 6(9), 746–750, doi:10.1038/ngeo1898.
- Pettit, E. C., and E. D. Waddington (2003), Ice flow at low deviatoric stress, *J. Glaciol.*, 49(166), 359–369.
- Phillips, T., H. Rajaram, W. Colgan, K. Steffen, and W. Abdalati (2013), Evaluation of cryo-hydrologic warming as an explanation for increased ice velocities in the wet snow zone, Sermeq Avannarleq, West Greenland, *J. Geophys. Res. Earth Surf.*, 118, 1241–1256, doi:10.1002/jgrf.20079.
- Poinar, K. M., I. Joughin, S. B. Das, M. B. Behn, J. T. M. Lenaerts, and M. R. van den Broeke (2015), Limits to future expansion of surface-melt-enhanced ice flow into the interior of western Greenland, *Geophys. Res. Lett.*, 42, 1800–1807, doi:10.1002/2015GL063192.
- Price, S. F., A. J. Payne, G. A. Catania, and T. A. Neumann (2008), Seasonal acceleration of inland ice via longitudinal coupling to marginal ice, *J. Glaciol.*, 54(185), 213–219.
- Price, S. F., A. J. Payne, I. M. Howat, and B. E. Smith (2011), Committed sea-level rise for the next century from Greenland Ice Sheet dynamics during the past decade, *Proc. Natl. Acad. Sci. U.S.A.*, 108(22), 8978–8983, doi:10.1073/pnas.1017313108.
- Rignot, E., and J. Mouginot (2012), Ice flow in Greenland for the International Polar Year 2008–2009, *Geophys. Res. Lett.*, 39, L11501, doi:10.1029/2012GL051634.
- Rogozhina, I., Z. Martinec, J. M. Hagedoorn, M. Thomas, and K. Fleming (2011), On the long-term memory of the Greenland Ice Sheet, *J. Geophys. Res.*, 116, F01011, doi:10.1029/2010JF001787.
- Rogozhina, I., J. M. Hagedoorn, Z. Martinec, K. Fleming, O. Soucek, R. Greve, and M. Thomas (2012), Effects of uncertainties in the geothermal heat flux distribution on the Greenland Ice Sheet: An assessment of existing heat flow models, *J. Geophys. Res.*, 117, F02025, doi:10.1029/2011JF002098.
- Rogozhina, I., A. G. Petrunin, A. P. M. Vaughan, B. Steinberger, J. V. Johnson, M. K. Kaban, R. Calov, F. Rickers, M. Thomas, and I. Koulakov (2016), Melting at the base of the Greenland Ice Sheet explained by Iceland hotspot history, *Nat. Geosci.*, 9, 366–369, doi:10.1038/ngeo2689.
- Ryser, C., M. P. Lüthi, L. C. Andrews, M. J. Hoffman, G. A. Catania, R. L. Hawley, T. A. Neumann, and S. S. Kristensen (2014a), Sustained high basal motion of the Greenland Ice Sheet revealed by borehole deformation, *J. Glaciol.*, 60(222), 647–660, doi:10.3189/2014JoG13J196.
- Ryser, C., M. P. Lüthi, L. C. Andrews, G. A. Catania, M. Funk, R. Hawley, M. Hoffman, and T. A. Neumann (2014b), Caterpillar-like ice motion in the ablation zone of the Greenland Ice Sheet, *J. Geophys. Res. Earth Surf.*, 119, 2258–2271, doi:10.1002/2013JF003067.
- Scambos, T. A., and T. Haran (2002), An image-enhanced DEM of the Greenland Ice Sheet, *Ann. Glaciol.*, 34, 291–298.
- Schroeder, D. M., D. D. Blankenship, and D. A. Young (2013), Evidence for a water system transition beneath Thwaites Glacier, West Antarctica, *Proc. Natl. Acad. Sci. U.S.A.*, 110(30), 12,225–12,228, doi:10.1073/pnas.1302828110.
- Schroeder, D. M., D. D. Blankenship, D. A. Young, and E. Quartini (2014), Evidence for elevated and spatially variable geothermal flux beneath the West Antarctic Ice Sheet, *Proc. Natl. Acad. Sci. U.S.A.*, 111(25), 9070–9072, doi:10.1073/pnas.1405184111.
- Schroeder, D. M., C. Grima, and D. D. Blankenship (2016), Evidence for variable grounding-zone and shear-margin basal conditions across Thwaites Glacier, West Antarctica, *Geophysics*, 81(1), WA35–WA43, doi:10.1190/GEO2015-0122.1.
- Sergienko, O., T. T. Creyts, and R. C. A. Hindmarsh (2014), Similarity of organized patterns in driving and basal stresses of Antarctic and Greenland Ice Sheets beneath extensive areas of basal sliding, *Geophys. Res. Lett.*, 41, 3925–3932, doi:10.1002/2014GL059976.
- Seroussi, H., M. Morlighem, E. Rignot, A. Khazendar, E. Larour, and J. Mouginot (2013), Dependence of century-scale projections of the Greenland Ice Sheet on its thermal regime, *J. Glaciol.*, 59(218), 1024–1034, doi:10.3189/2013JoG13J054.
- Shannon, S. R., et al. (2013), Enhanced basal lubrication and the contribution of the Greenland Ice Sheet to future sea-level rise, *Proc. Natl. Acad. Sci. U.S.A.*, 110(35), 14,156–14,161, doi:10.1073/pnas.1212647110.
- Shapiro, N. M., and M. H. Ritzwoller (2004), Inferring surface heat flux distributions guided by a global seismic model: Particular application to Antarctica, *Earth Planet. Sci. Lett.*, 223, 213–224, doi:10.1016/j.epsl.2004.04.011.
- Tarasov, L., and W. R. Peltier (2003), Greenland glacial history, borehole constraints, and Eemian extent, *J. Geophys. Res.*, 108(B3), 2143, doi:10.1029/2001JB001731.
- Tedstone, A. J., P. W. Nienow, N. Gourmelen, A. Dehecq, D. Goldberg, and E. Hanna (2015), Decadal slowdown of a land-terminating sector of the Greenland Ice Sheet despite warming, *Nature*, 526, 692–695, doi:10.1038/nature15722.
- Thomsen, H. H., O. B. Olsen, R. J. Braithwaite, and C. Bøggild (1991), Ice drilling and mass balance at Pakitsoq, Jakobshavn, central West Greenland, *Grønlands Geologiske Undersøgelse*, Copenhagen, Denmark.
- van de Wal, R. S. W., W. Boot, M. R. van den Broeke, C. J. P. P. Smeets, C. H. Reijmer, J. J. A. Donker, and J. Oerlemans (2008), Large and rapid melt-induced velocity changes in the ablation zone of the Greenland Ice Sheet, *Science*, 321, 111–113, doi:10.1126/science.1158540.
- van der Veen, C. J., T. Leftwich, R. von Frese, B. M. Csatho, and J. Li (2007), Subglacial topography and geothermal heat flux: Potential interactions with drainage of the Greenland Ice Sheet, *Geophys. Res. Lett.*, 34, L12501, doi:10.1029/2007GL030046.
- van der Veen, C. J., Y. Ahn, B. M. Csatho, E. Mosley-Thompson, and W. B. Krabill (2009), Surface roughness over the northern half of the Greenland Ice Sheet from airborne laser altimetry, *J. Geophys. Res.*, 114, F01001, doi:10.1029/2008JF001067.

- Waddington, E. D., H. Conway, E. J. Steig, R. B. Alley, E. J. Brook, K. C. Taylor, and J. W. C. White (2005), Decoding the dipstick: Thickness of Siple Dome, West Antarctica, at the Last Glacial Maximum, *Geology*, 33(4), 281–284, doi:10.1130/G21165.1.
- Waddington, E. D., T. A. Neumann, M. R. Koutnik, H.-P. Marshall, and D. L. Morse (2007), Inference of accumulation-rate patterns from deep layers in glaciers and ice sheets, *J. Glaciol.*, 53(183), 694–712.
- Weertman, J. (1968), Comparison between measured and theoretical temperature profiles of the Camp Century, Greenland, borehole, *J. Geophys. Res.*, 73, 2691–2700, doi:10.1029/JB073i008p02691.
- Willis, M. J., B. G. Herreid, M. G. Bevis, and R. E. Bell (2015), Recharge of a subglacial lake by surface meltwater in northeast Greenland, *Nature*, 518, 223–227, doi:10.1038/nature14116.
- Wolovick, M. J., and T. T. Creyts (2016), Overturned folds in ice sheets: Insights from a kinematic model of traveling stick patches and comparisons with observations, *J. Geophys. Res. Earth Surf.*, 121, 1065–1083, doi:10.1002/2015JF003698.
- Wolovick, M. J., T. T. Creyts, W. R. Buck, and R. E. Bell (2014), Traveling slippery patches produce thickness-scale folds in ice sheets, *Geophys. Res. Lett.*, 41, 8895–8901, doi:10.1002/2014GL062248.
- Zwally, H. J., M. B. Giovinetto, M. A. Beckley, and J. L. Saba (2012), Antarctic and Greenland drainage systems. [Available at http://icesat4.gsfc.nasa.gov/cryo_data/ant_grn_drainage_systems.php.]